PAPER

Check for updates

Heterogeneity of the vanadia phase dispersed on titania. Co-existence of distinct mono-oxo VOx sites

Theocharis Kentri,[a,b] Athanasios Tsevis[c] and Soghomon Boghosian ⓘ *[a,b,c]

The structural and configurational characteristics of the species comprising the $(VO_x)_n$ phase dispersed on $TiO_2(P25)$ are studied under oxidative dehydration conditions by *in situ* molecular vibrational spectroscopy (Raman, FTIR) complemented by *in situ* Raman/^{18}O isotope exchange and Raman spectroscopy under static equilibrium at temperatures of 175–430 °C and coverages in the 0.40–5.5 V nm^{-2} range. It is found that the dispersed $(VO_x)_n$ phase consists of distinct species with different configurations. At low coverages of 0.40 and 0.74 V nm^{-2}, isolated (monomeric) species prevail. Two distinct mono-oxo species are found: (i) a majority Species-I, presumably of distorted tetrahedral $O=V(-O-)_3$ configuration with $V=O$ mode at 1022–1024 cm^{-1} and (ii) a minority Species-II, presumably of distorted octahedral-like $O=V(-O-)_4$ configuration with $V=O$ mode at 1013–1014 cm^{-1}. Cycling the catalysts in the 430 → 250 → 175 → 430 °C sequence results in temperature-dependent structural transformations. With decreasing temperature, a Species-II → Species-I transformation with concomitant surface hydroxylation takes place by means of a hydrolysis mechanism mediated by water molecules retained by the surface. A third species (Species-III, presumably of di-oxo configuration with ν_s/ν_{as} at ~995/985 cm^{-1}) occurs in minority and its presence is increased when further lowering the temperature according to a Species-I → Species-III hydrolysis step. Species-II ($O=V(-O-)_4$) shows the highest reactivity to water. For coverages above 1 V nm^{-2}, an association of VOx units takes place leading to gradually larger polymeric domains when the coverage is increased in the 1.1–5.5 V nm^{-2} range. Polymeric $(VO_x)_n$ domains comprise building units that maintain the structural characteristics (termination configuration and V coordination number) of Species-I, Species-II, and Species-III. The terminal $V=O$ stretching modes are blue-shifted with increasing $(VO_x)_n$ domain size. A lower extent of hydroxylation is evidenced under static equilibrium forced dehydrated conditions, thereby limiting the temperature dependent structural transformations and excluding the possibility of incoming water vapors as the cause for the temperature dependent effects observed in the *in situ* Raman/FTIR spectra. The results address open issues and offer new insight in the structural studies of VOx/TiO2 catalysts.

1. Introduction

A wide range of catalytic processes of industrial and environmental interest benefit from supported vanadia catalysts.[1,2] Worth mentioning are the selective catalytic reduction (SCR) of NO_x with NH_3,[3–7] the partial oxidation of methane,[8] the partial oxidation of methanol,[9] the oxidative dehydrogenation of light alkanes,[10] and the selective oxidation of butane.[11]

Research on the molecular structure and catalytic performance of titania-supported vanadia catalysts, widely used in the NH_3–SCR NO_x removal process, is of topical interest[12] due to

new legislation-driven restrictions on NO_x emissions. Vanadia-based SCR catalysts typically also contain tungsta but model studies still focus on the V_2O_5/TiO_2 system.[12–14] Despite the very extensive research efforts on revealing the coordination of the V atom, the termination configuration (mono-oxo *vs.* di-oxo), the vibrational properties and assignments of V–O modes, the extent of association (monomeric *vs.* polymeric species) *etc.*, the structural properties of the dispersed $(VO_x)_n$ sites are under debate.[7,15–25] Fundamental interest is uninterruptedly focused on identifying the $(VO_x)_n$ configurational characteristics to help determine the dispersed phase composition and understand the reaction mechanism at the molecular level.

Surprisingly, the issue of the dispersed phase $(VO_x)_n$ heterogeneity remains underestimated and recent comprehensive reviews on the systematics of supported transition metal oxides report over simplified descriptions for the dispersed

[a]Department of Chemical Engineering, University of Patras, Patras, Greece.
E-mail: bogosian@chemeng.upatras.gr
[b]Institute of Chemical Engineering Sciences, FORTH/ICE-HT, Patras, Greece
[c]School of Science and Technology, Hellenic Open University, GR-26335 Patras, Greece

phase structure of titania-supported vanadia catalysts.[6,26] However, the diversity of reported proposed configurations (*e.g.* pyramidal O=VO$_4$,[21] tetrahedral O=VO$_3$,[27] and/or pertinent variations depending on the coverage) reflects the complexity of the structure, suggesting that one cannot exclude the fact that the dispersed (VO$_x$)$_n$ phase is heterogeneous, even at low coverage. Outstanding paradigms of spectroscopically evidenced heterogeneity of oxo-metallic phases dispersed on TiO$_2$ include the existence of distinct mono-oxo and di-oxo ReO$_x$ sites,[28] reversible temperature-dependent transformations between MoO$_x$ species,[29,30] and the existence of distinct mono-oxo WO$_x$ species.[31] Additional examples of dispersed oxo-metallic phase heterogeneity on other supports (*e.g.* SiO$_2$, Al$_2$O$_3$, CeO$_2$) can also be found in the literature on supported transition metal oxide catalysts.[32–38]

Significantly, attention in experimental *in situ* spectroscopic studies is focused on dehydrated conditions, *i.e.* without the presence of H$_2$O(g) in the gas feed (hereinafter referred to as *dehydrated feed conditions*). However, it has become widely accepted that water is a ubiquitous molecule and that fully dehydrated dispersed vanadia on titania occurs only under severe conditions (*e.g.* vacuum) of the absence of absolute water.[19,20,39,40] As a paradigm, water molecules formed as a result of the titration of surface hydroxyls by the V precursor species[41] during the deposition preparation step can be retained on the titania surface by H-bonds.[31] Therefore, the state of a catalyst under dehydrated feed conditions should rather be described as hydroxylated, since the dissociative adsorption of extant water molecules would result in OH formation, *e.g.* by protonation of O atoms along V–O–Ti anchoring bonds.[39,40] Such hydroxylated VO$_x$ species dispersed on TiO$_2$ facets are proposed as plausible stable sites based on theoretical and Density Functional Theory (DFT) calculations.[19,20,23,25]

With relevance to the issue of heterogeneity of the VO$_x$ dispersed phase on titania anatase, theoretical and experimental studies suggest that the dispersed phase is inhomogeneous with structurally varying vanadia species on various TiO$_2$ facets.[12,23,25,42,43] Pertinent catalytic properties have also been reported to be dependent on the titania crystal structure.[44–46] Likewise, atomic scale redox dynamics in anatase supported V$_2$O$_5$-based catalysts were found to be dependent on anatase surface terminations.[47] One of the most fascinating findings suggests the occurrence of tetrahedral-like tetra-coordinated O=VO$_2$OH on the anatase (101) facet and octahedral-like penta-coordinated O=VO$_3$OH on the anatase (001) facet.[23,25] Importantly, Arnarson *et al.*, based on DFT calculations, have shown that the role of the support is not solely to enable the formation of a dispersed oxo-vanadium phase, but also to prescribe its conformational characteristics and thereby its functional behavior.[25]

The aim of the present work is to clarify the issue of heterogeneity within the (VO$_x$)$_n$ phase dispersed on titania under dehydrated feed conditions (*i.e.* without H$_2$O(g) present in the feed) by applying the criteria of molecular vibrational spectroscopy.[48–50] To this end, *in situ* Raman and FTIR spectroscopies (the latter in the overtone region), *in situ* Raman/^{18}O

isotope exchange studies as well as high temperature Raman spectroscopy in static equilibrium under forced dehydrated conditions (*i.e.* sampling under O$_2$(g) after 1 h evacuation at 200 °C) are brought into effective action to identify existing structurally distinct sites. Industrial Degussa (P25) is chosen as the support, providing a richness of facets (*i.e.* anatase (101), (100), (001) and rutile (110))[51,52] and an abundance of defects, thereby favoring molecular as well as dissociative adsorption of retained water molecules. The forced dehydrated conditions applied were found to limit those temperature-dependent effects that were attributed to dissociative water adsorption taking place upon cooling. The results and the discussion address the aspects of vanadium coordination, termination configuration (*e.g.* mono-oxo *vs.* di-oxo), and site nuclearity (isolated *vs.* associated species) and contribute to an improved understanding of temperature and coverage effects on the structural properties of titania-supported vanadia catalysts.

2. Experimental section

2.1. Preparation and textural characterization of VO$_x$/TiO$_2$ catalysts

The equilibrium–deposition–filtration (EDF) method[51] was used for the synthesis of VO$_x$/TiO$_2$ samples with surface densities of 0.40–5.5 V nm^{-2}, *i.e.* below the experimentally determined monolayer coverage of 7–8 V nm^{-2}.[15] Industrial Degussa P25, marketed as consisting of 80 wt% anatase and 20% wt% rutile with a typical composition of 78% anatase, 14% rutile and 8% of an amorphous phase,[54] was the support used and NH$_4$VO$_3$ (Alfa Aesar, 99%) was the vanadia precursor. The synthesis of each sample was designed at a specific precursor solution concentration (in the range $C_{V(V), initial}$ = 0.68 × 10^{-3}–43.6 × 10^{-3} M) and precursor solution pH (controlled at pH = 9 or 5, see Table 1) adjusted and controlled automatically with a Radiometer Copenhagen ABU901 autoburette. Following the equilibration (24 h) of the support/precursor solution system, the filtration procedure took place to obtain wet H$_K$V$_X$O$_Y$$^{Z-}$/TiO$_2$(P25) paste samples that were dried for 16 h at 120 °C and calcined in a muffle furnace at 480 °C for 4 h under static air. The vanadium surface concentration for all samples was calculated by determining spectrophotometrically the equilibrium V(v) concentration (*i.e.* in the filtrate). Further details of the procedure have earlier been thoroughly

Table 1 Characteristics of VO$_x$/TiO$_2$ catalysts (V surface density, initial concentration of the precursor solution, pH values of the impregnation solution and the BET specific surface area. Calcination, 480 °C, 4 h. Specific surface area of calcined bare TiO$_2$(P25) = 49 m^2 g^{-1}

Catalysts	n_s (V nm^{-2})	$C_{V(V), initial}$ (M)	pH	S_{BET} (m^2 g^{-1})
0.40VTiO$_2$(P25)	0.40	6.8 × 10^{-4}	9	48
0.74VTiO$_2$(P25)	0.74	1.2 × 10^{-3}	9	48
1.1VTiO$_2$(P25)	1.1	2.5 × 10^{-3}	9	48
2.0VTiO$_2$(P25)	2.0	6.0 × 10^{-3}	9	48
4.0VTiO$_2$(P25)	4.0	2.0 × 10^{-2}	5	48
5.5VTiO$_2$(P25)	5.5	4.4 × 10^{-2}	5	48

described.[53,55] The specific surface area (BET surface area, S_{BET}) of the catalysts was determined after calcination by nitrogen adsorption–desorption.[55] The coverage, expressed in terms of V nm^{-2}, is calculated for each sample based on the specific surface area and the percent V content. Table 1 compiles the characteristics of the VO$_x$/TiO$_2$ samples, which are denoted as xVTiO$_2$(P25) where x is the V surface density (V nm^{-2}).

2.2. Raman and FTIR spectroscopy. Protocols of measurements

2.2.1. *In situ* steady state Raman spectra under dehydrated feed conditions.
The *in situ* Raman spectra of the VO$_x$/TiO$_2$(P25) catalyst samples were recorded using a homemade optical Raman cell that has earlier been described in detail.[56,57] Typically, 130–140 mg of each sample in powder form was pressed into a wafer by using a hydraulic press at a ~25 kN load. The wafer was mounted on the sample holder of the *in situ* cell and heated for 1 h to 430 °C under a 30 cm^3 min^{-1} flow of dry 20% O$_2$/He feed gas (He 99.999% and O$_2$ 99.999% from L′ Air Liquide). A 491.5 nm (cyan) line of a Cobolt Calypso DPSS laser was used for exciting the Raman spectra, operated at a power of ~10 mW at the sample wafer. Additionally, to limit the irradiance, the incoming beam was slightly defocused by a cylindrical lens, thereby resulting in a ~2 mm^2 spot size on the sample. A horizontal scattering plane with right angle scattered radiation collection was set as optical geometry. A 1403 Spex 0.85 m double monochromator was used to analyse the scattered light and a −20 °C-cooled RCA photomultiplier tube interfaced with the Labspec software was used as a detector.

Recording of *in situ* Raman spectra under dehydrated feed conditions started at 430 °C. The temperature was subsequently lowered to 250 °C and 175 °C under a continuous flow of the dry 20% O$_2$/He feed gas, and steady-state *in situ* Raman spectra were collected after 1 h and 45 min of sample treatment at each temperature. The temperature was then raised to 430 °C and the catalyst structural state reinstatement was checked and confirmed by reproducing the *in situ* Raman spectrum at 430 °C. The resolution was set at 7 cm^{-1}. To obtain a high signal-to-noise ratio, a slow scan speed with 1.2 s photon counting per point at increments of 0.25 cm^{-1} was implemented. The obtained Raman spectra were normalised as described earlier in detail[30,58] to account for the "path length" effect caused by the wide 0.40–5.5 V nm^{-2} coverage range of the samples studied.

2.2.2. *In situ* steady state FTIR spectra under dehydrated feed conditions.
In situ FTIR spectra in the steady state were recorded using a Spectra Tech DRIFT *in situ* cell on a Nicolet 6700 FTIR spectrometer equipped with a KBR beam splitter and an MCTB detector. The measurements' protocol was identical to the one followed for the *in situ* Raman study. Hence, each sample was first treated for 1 h at 430 °C under a flow of dry 20% O$_2$/He gas (at a flow of 30 cm^3 min^{-1}) before recording the *in situ* FTIR spectrum at 430 °C. The resolution was 4 cm^{-1} and 64 scans were averaged for each spectrum. The temperature was then cycled at 430 → 250 → 175 → 430 °C and *in situ* FTIR spectra in the steady state were recorded at each tempera-

ture. Reinstatement of the structural conditions at 430 °C was confirmed by reproducing the pertinent spectrum. *In situ* FTIR spectra at each temperature were also recorded for pure TiO$_2$(P25). Finally, due to strong absorption in the fundamental V=O stretching spectral range, the overtone V=O spectral region is exploited.

2.2.3. *In situ* Raman/^{18}O isotope exchange study.
The protocol followed for undertaking the *in situ* Raman–^{18}O/^{16}O exchange measurements at 425 °C was established by using 11% H$_2$/He (H$_2$ 99.999% from L′ Air Liquide) and 2% ^{16}O$_2$/He gas mixtures as the reductant and oxidant, respectively, as described earlier.[59,60] It turned out that 1–2 min of reduction by exposure to the 11% H$_2$-containing gas were sufficient for an adequate reduction, whilst 8 min were necessary for re-oxidation by exposure to the 2% O$_2$-containing gas. Hence, each reduction/oxidation ^{18}O/^{16}O isotope exchange cycle consisted of a 1–2 min reduction under flowing 11% H$_2$/He and an 8 min oxidation under flowing 2% ^{18}O$_2$/He (Linde, certified mixture). Each studied sample was subjected to up to 21 isotope exchange cycles and *in situ* Raman spectra were recorded after each ^{18}O/^{16}O isotope exchange cycle at 425 °C.

2.2.4. Raman spectra under forced dehydrated static equilibrium conditions.
The concept of the herein described neoteric experiments has recently been described.[30,31] The objectives for studying the high temperature Raman spectra of VO$_x$/TiO$_2$ catalysts under forced dehydrated static equilibrium conditions are threefold. First, to examine if the temperature-dependent transformations induced by dissociative H$_2$O adsorption upon cooling in the 430 → 175 °C range can be limited; second, to examine if the dispersed VO$_x$ phase heterogeneity can still be confirmed under forced dehydration conditions; and third, to exclude the possibility of incoming H$_2$O (g) as the cause of the effects observed in the *in situ* Raman and FTIR studies.

For preparing the samples, 30–50 mg of each studied xVTiO$_2$(P25) catalyst was filled into a quartz optical cell that has been described in detail recently.[29,30] Very briefly,[30,31] the quartz cell had a 20 mm o.d. ~3 cm long main compartment, a 6 mm o.d. ~2 cm long bottom appendix for containing the catalyst powder and a 6 mm o.d. ~3 cm long top stem. Each cell, filled with the catalyst powder was attached to a T-shape glass container ($V \sim 43$ cm^3) and to a vacuum line, as shown in Fig. 1. The cell, while being heated at 200 °C for 1 h,[30,31] was subjected to dynamic vacuum (~10^{-4} atm) with the vacuum line trap immersed in liquid nitrogen for condensing water molecules forcibly removed from the sample. The vacuum line was then isolated from the vacuum pump and oxygen gas (Linde, 99.999%) was injected and allowed to reach equilibrium with liquid oxygen condensed in the liquid nitrogen trap ($p_{O_2} = 0.19$ atm, *i.e.* the vapor pressure of oxygen at 77 K). Valve V1 (Fig. 1) was then closed, and the amount of oxygen gas contained in the T-shape construction (~3.3 × 10^{-4} mol) was condensed in the quartz cell appendix by surrounding the cell appendix bottom with a liquid nitrogen containing dewar. The quartz cell was then sealed at its stem at a final volume of ~8 cm^3 with a propane/oxygen torch, hence at a final oxygen
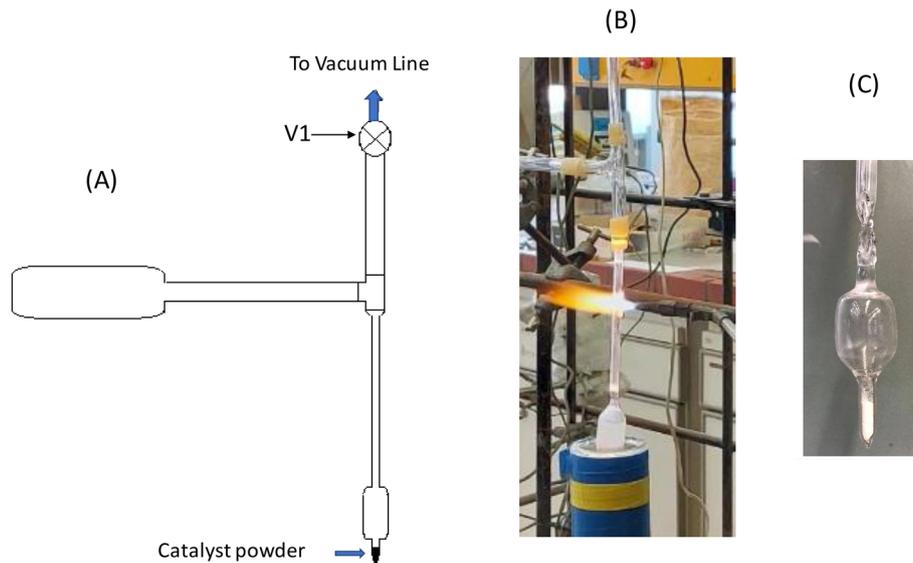
Fig. 1 (A) Diagram of the T-like construction and the quartz cell containing the sample, attached to the vacuum line; (B) picture of the quartz cell appendix immersed in liquid nitrogen for condensing the O_2 injected in the line; sealing of the cell by an oxygen–propane torch; (C) the sealed cell containing the catalyst powder and oxygen gas, $p_{O_2, 298 K} \sim 1$ atm.

pressure of $p_{O_2, 298 K} \sim 1$ atm under static forced dehydrated oxidative conditions. The ratio of moles $O_2(g)$ added to the cell vs. the moles V contained in the sample was in the range of $\frac{n_{O_2(g)}}{n_V} = 70 - 100$, thereby ensuring that vanadium will remain in the +5 oxidation state.

For recording the Raman spectra, each cell was placed into an optical furnace[61,62] and irradiated by a linearly polarized green 532.0 nm line of a Spectra Physics Excelsior DPSS laser operated at ~15 mW on the catalyst sample. The scattered light was collected at 90° through an edge filter, analyzed by an IHR-320 JY, ISA-Horriba Group monochromator and detected by a −56 °C thermoelectrically cooled CCD interfaced with the Labspec software. The spectral resolution was set to 2 cm^{-1}. A detailed description of the instrumentation is given elsewhere.[63] Raman spectra under static equilibrium were first recorded at 430 °C and subsequently at a sequence of decreasing temperatures at 250, 175 and 120 °C. Finally, the temperature was raised to 430 °C for reproducing the pertinent Raman spectrum. Raman spectra under forced dehydrated static equilibrium were recorded for samples with coverage in the range 0.40–2.0 V nm^{-2}. For coverages of 4.0 and 5.5 V nm^{-2}, strong scattering from the quartz walls of the sealed container cells did not allow recording of Raman spectra.

3. Results and discussion

3.1. Heterogeneity of the VO_x phase dispersed on $TiO_2(P25)$ at low coverage. Vibrational (Raman and IR) properties and the configuration of prevailing species

3.1.1. Temperature dependence of the V–O stretching region, heterogeneity of the VO_x phase and structural impli-

cations. Fig. 2 and 3 show the temperature dependence of the in situ Raman spectra (panels (A)), the in situ FTIR spectra (panels (B)) and the static equilibrium Raman spectra (panels (C)) obtained for the low-loaded 0.40 and 0.74 V nm^{-2} $VO_x/TiO_2(P25)$ catalysts. The in situ Raman and FTIR spectra are recorded under flowing 20% O_2/He dry feed gas, whilst the static equilibrium Raman spectra are recorded in sealed quartz cells under a static oxygen atmosphere (see the Experimental section). The spectra shown in each panel are recorded at a sequence of decreasing temperatures. After recording the temperature-dependent sequential spectra, the spectrum at 430 °C was reproduced in each case. It is noteworthy that the choice of excitation wavelength for the Raman spectra (i.e. cyan 491.5 nm in panels (A) and green 532.0 nm in panels (C)) had no influence on the Raman spectra for the studied $VO_x/TiO_2(P25)$ catalysts with low coverage.

The main Raman band in the V–O stretching region shown in Fig. 2(A) and 3(A) is asymmetric, displaying at least one additional component at its low wavenumber side. This observation is confirmed by the in situ FTIR spectra shown in Fig. 2(B) and 3(B), which are recorded in the overtone region thereby resulting in an approximate doubling of bands' distances and a clear separation of the overtone counterparts (i.e. at 2031 and ~2010 cm^{-1} for 0.40 V nm^{-2} and at 2034 and 2012 cm^{-1} for 0.74 V nm^{-2}). Hence, in Fig. 2(A) and 3(A) two distinct bands are also noted as band (I) at 1023–1024 cm^{-1} and band (II) at ~1013–1014 cm^{-1} whereas a third feature (III), consisting probably of two components, is also discerned at 995/985 cm^{-1}, of which the overtones are observed in the 1985–1960 cm^{-1} range (Fig. 2(B) and 3(B)). Similar observations of multiple bands are exhibited in Fig. 2(C) and 3(C) under static equilibrium, namely band (I) at 1025 and 1027 cm^{-1}, band (II) at ~1014 and ~1016 cm^{-1} and double band (III) at ~995/985 cm^{-1}.

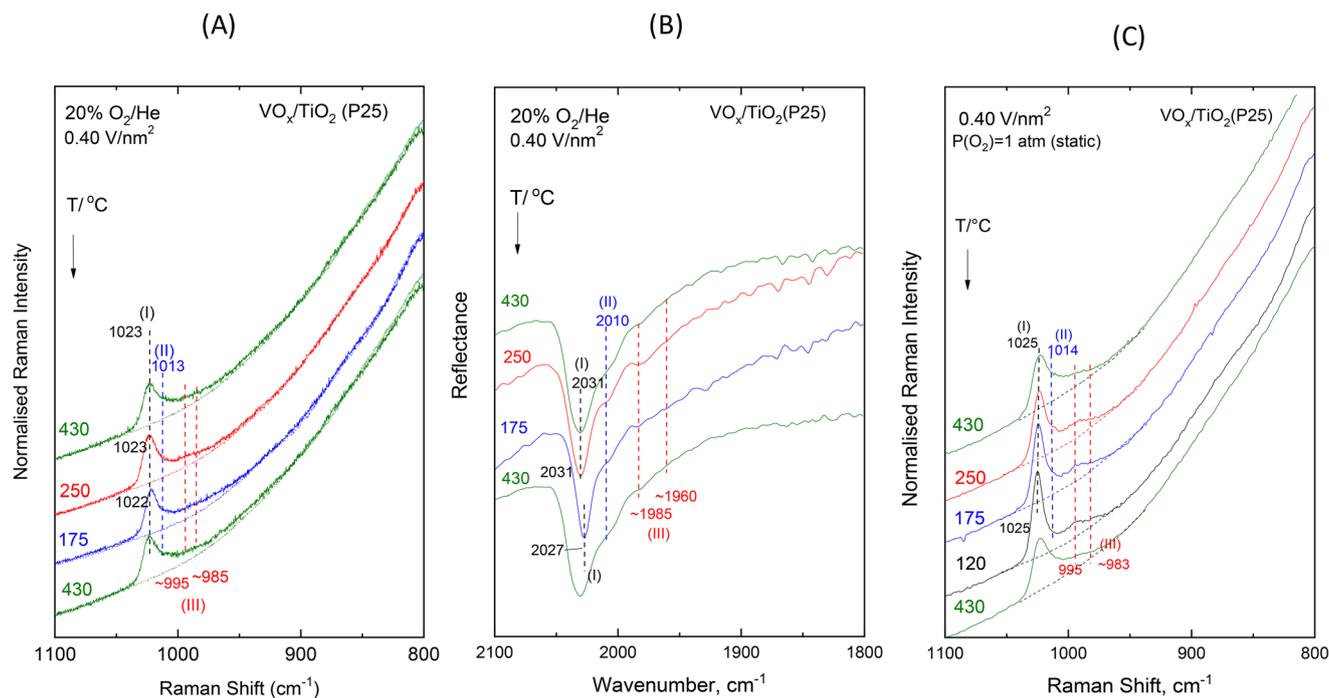**Fig. 2** VO_x/TiO_2(P25) with a surface density of 0.40 V nm^{-2}: (A) sequential (430 → 250 → 175 → 430 °C) *in situ* Raman spectra obtained under flowing 20%O_2/He at temperatures as indicated by each spectrum. Dashed traces: TiO_2(P25) spectra. Recording parameters: laser wavelength, λ_0 = 491.3 nm; laser power, w = 10 mW; time constant, τ = 1.2 s; spectral slit width, ssw = 7 cm^{-1}. (B) Sequential (430 → 250 → 175 → 430 °C) *in situ* FTIR spectra obtained under flowing 2%O_2/He at temperatures as indicated by each spectrum, resolution, 4 cm^{-1}. (C) Sequential (430 → 250 → 175 → 120 → 430 °C) Raman spectra at static equilibrium under $p_{O_2, \, 300 \, K}$ = 1 atm at temperatures as indicated by each spectrum. Dashed lines: TiO_2(P25) spectra. Recording parameters: λ_0 = 532.0 nm; laser power, w = 15 mW; resolution, 2 cm^{-1}.

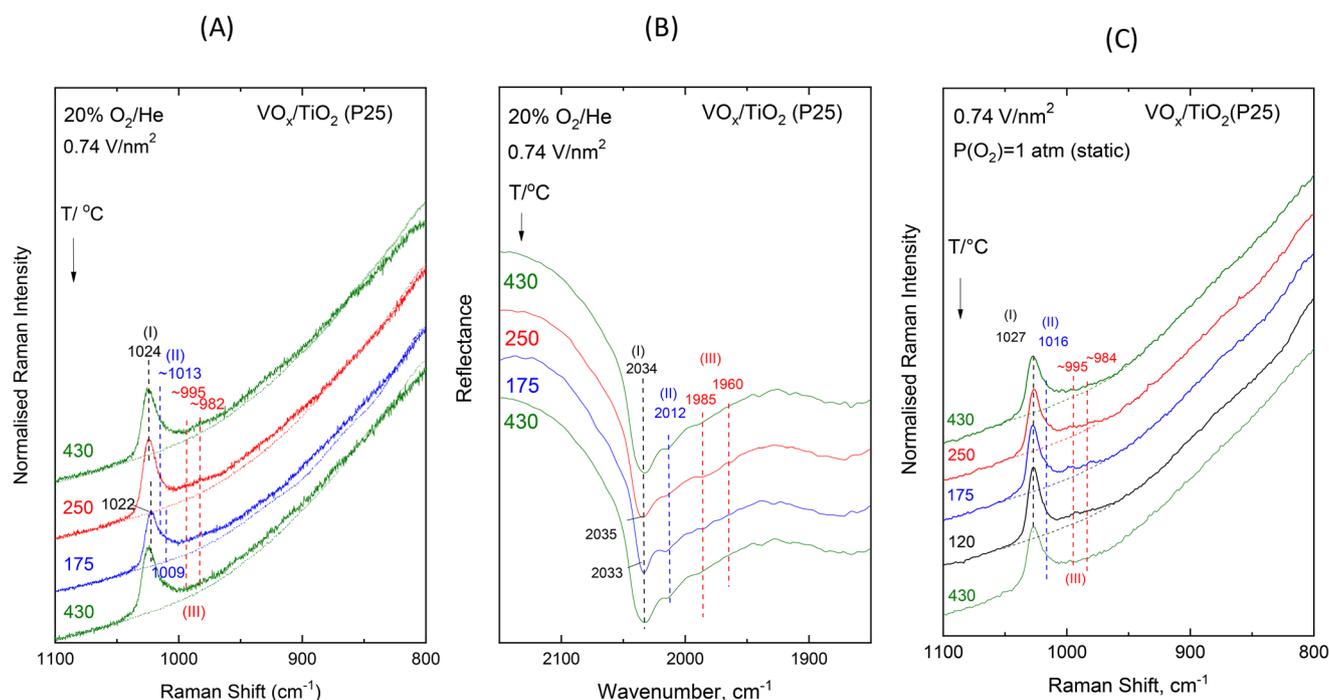**Fig. 3** VO_x/TiO_2(P25) with a surface density of 0.74 V nm^{-2}: (A)–(C) see the caption to Fig. 2. Spectral recording parameters: see the Fig. 2 caption.

The temperature-dependent features in Fig. 2 and 3 show that upon cooling, the band (II) intensity is weakened relative to the band (I) intensity, thereby evidencing that bands (I) and (II) originate from two distinct species. The pertinent observation is particularly noticeable under forced dehydrated conditions in the Raman spectra under static equilibrium, *i.e.* Fig. 2(C) and 3(C). Hence, band (I) is assigned to a majority Species (I) and band (II) is assigned to a minority Species (II). Before addressing the assignment of bands (III) we examined the degree of association (*i.e.* isolated/monomer *vs.* associated/polymeric) and termination configuration (*i.e.* mono-oxo *vs.* di-oxo) for the distinct Species (I) and Species (II).

3.1.2. Extent of association of dispersed VO_x sites. Fig. 4 shows the *in situ* Raman spectra obtained at 430 °C for the xVTiO$_2$(P25) catalysts for various coverages in the range 0.40–5.5 V nm^{-2}. The corresponding *in situ* Raman spectrum of pure TiO$_2$(P25) is also shown as a dashed background under each spectrum. With increasing coverage, a broad band feature at ~915 cm^{-1} is discerned in the spectrum obtained for the 1.1VTiO$_2$(P25) sample, which progressively gains intensity and undergoes a blue shift to ~930 cm^{-1} with increasing coverage in the 1.1–5.5 V nm^{-2} range. This is a common and very often reported observation[7,20,64–67] in the literature on Raman studies pertaining to titania-supported vanadia catalysts. Although the assignment of the broad 930 cm^{-1} band has raised controversy in the literature,[68] the band's growth with increasing coverage has been related to the increase of the polymeric $(VO_x)_n$ sites' population and thereby assigned to V–O–V or O–V–O bridging functionalities (either $\nu_{as,\ V-O-V}$ or $\nu_{s,\ O-V-O}$).[7,20,40,49,64–66,69–73] Moreover, both theoretical (molecular dynamics and DFT calculations) and experimental studies report that isolated (monomeric) species prevail at coverages typically below 2 V nm^{-2}.[19,25,67]

The assignment of the 915–930 cm^{-1} bands to the V–O–V bridging modes is justified by the absence of such a band at the lowest coverage of 0.40 V nm^{-2} and the increase of its intensity relative to the intensity of the 1024–1030 cm^{-1} V=O stretching mode, as seen clearly in Fig. 4. The ~915 cm^{-1} band is hardly observed also for the 0.74 V nm^{-2} coverage. Notably, the number of associative V–O–V links increases relative to the terminal V=O sites with increasing coverage thereby justifying a concomitant progress in the formation of polymer units. Hence, at coverages of 0.40 and 0.74 V nm^{-2} the dispersed VO_x phase consists exclusively of isolated monomeric species, *i.e.* both Species (I) and Species (II) are distinct monomeric species.

3.1.3. Termination configuration of prevailing Species (I) and (II). The band splitting pattern upon $^{18}O/^{16}O$ substitution and the pertinent vibrational isotope effects can shed light on the differentiation between dispersed oxometallic MO_x sites with different termination configurations (*i.e.* mono-oxo M=O, di-oxo M(=O)$_2$ *etc.*).[48,57,70] Fig. 5 (panels (A) and (B))
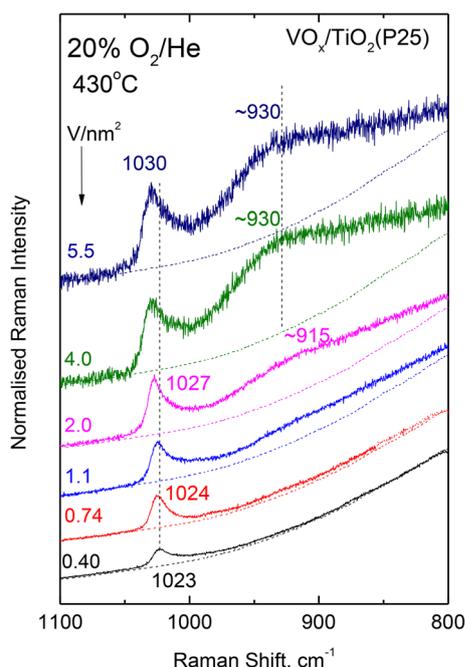

Fig. 5 Sequential *in situ* Raman spectra obtained at *T* = 425 °C under flowing 2% $^{18}O_2$/He after subsequent H$_2$/$^{18}O_2$ reduction/oxidation cycles as indicated by each spectrum. (A) VO$_x$/TiO$_2$(P25) with a surface density of 0.40 V nm^{-2}; (B) VO$_x$/TiO$_2$(P25) with a surface density of 0.74 V nm^{-2}. The corresponding *in situ* Raman spectra of TiO$_2$(P25) are subtracted from the spectra obtained for the samples. Spectral recording parameters: see the Fig. 2 caption.

Fig. 4 *In situ* Raman spectra obtained at *T* = 430 °C under flowing 20% O$_2$/He for VO$_x$/TiO$_2$(P25) catalysts with surface densities (V nm^{-2}) as indicated by each spectrum. Spectral recording parameters: see the Fig. 2 caption.
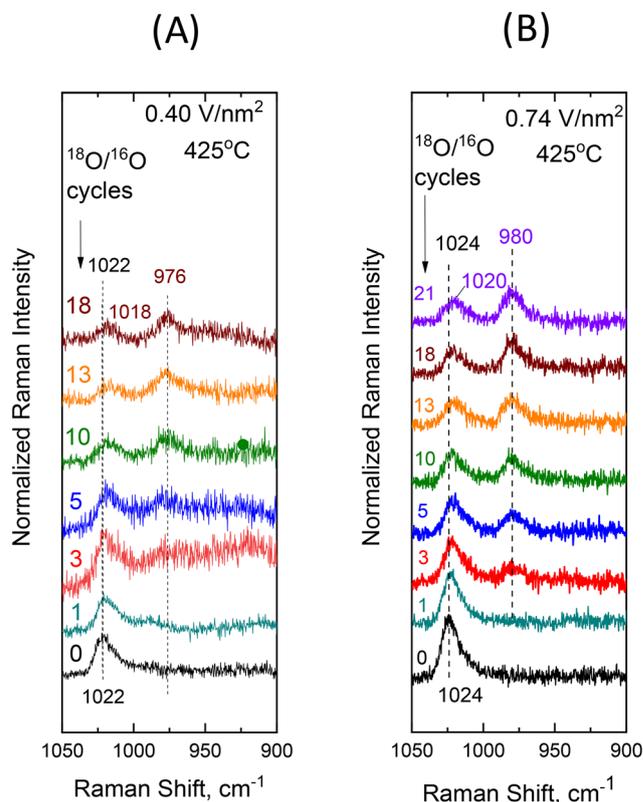
shows the evolution of the *in situ* Raman spectra obtained at 425 °C for the 0.40VTiO$_2$(P25) and 0.74VTiO$_2$(P25) samples upon successive ^{18}O/^{16}O isotope exchange cycles. The corresponding *in situ* Raman spectrum obtained for pure TiO$_2$(P25) under flowing 20% O$_2$/He is subtracted from the xVTiO$_2$(P25) spectra in each case. It is evident that a single isotopic band splitting is observed for both samples, thereby pointing to a mono-oxo termination configuration for the distinct monomeric Species-I and Species-II. The slight red shift observed for $\nu_{V=^{16}O}$ following the applied ^{18}O/^{16}O isotope exchange cycles (*i.e.* 1022 → 1018 cm^{-1} for 0.40VTiO$_2$(P25) and 1024 → 1020 cm^{-1} for 0.74VTiO$_2$(P25), Fig. 5(A) and (B)) is due to the vibrational isotope effect addressed earlier for WO$_x$/TiO$_2$ and MoO$_x$/TiO$_2$ catalysts.[31,54,56] The red shift observed for the V=^{16}O terminal mode is attributed to V–^{16}O–Ti → V–^{18}O–Ti substitution, by means of which higher basicity (electron-donating ability) is resulted for the ^{18}O atom of the anchoring bridge due to the lowering of the O atom electronegativity. Hence, a slight strengthening of the V–^{18}O(–Ti) bonds takes place, in turn resulting in a commensurate weakening of the unsubstituted V=^{16}O terminal sites.[31,57,59] Importantly, as seen in Fig. 5, the terminal V=^{16}O mode is already red-shifted from the first ^{18}O/^{16}O cycle, thereby indicating that the V–^{16}O–Ti → V–^{18}O–Ti substitution precedes the V=^{16}O → V=^{18}O substitution.[31,57,59]

A theoretical confirmation of the mono-oxo V=O termination configuration for both distinct monomeric Species-I and Species-II occurring in the dispersed VO$_x$ phase at low coverage (0.40 and 0.74 V nm^{-2}) can be obtained by adopting the diatomic model in the harmonic approximation and exploiting the 1022 and 1024 cm^{-1} values for the $\nu_{V=^{16}O}$ modes observed (Fig. 5). On the ground of equal V=^{16}O and V=^{18}O bond lengths and applying the isotopic ratio of 1.0452,[70] the calculated wavenumbers for the isotopically substituted V=^{18}O sites are 978 and 980 cm^{-1} in perfect agreement with the experimental observations of V=^{18}O band wavenumbers in Fig. 5. A synopsis of the calculations is compiled in Table 2.

Additional evidence pointing to the mono-oxo termination configuration for Species-I and Species-II comes from the exploitation of their respective V=O terminal stretching fundamental (Raman) and first overtone (IR) band wavenumbers. Hence, since anharmonicity is accountable for observing the $\nu_{2\leftarrow0}$ IR overtones, the following pertinent equations are con-

sidered in the diatomic approximation:[57,74,75]

$$\nu_{V=O,1\leftarrow0(R)} = \omega_{e,V=O}(1 - 2\chi_{e,V=O})$$

$$\nu_{V=O,2\leftarrow0(IR)} = 2\omega_{e,V=O}(1 - 3\chi_{e,V=O})$$

where $\omega_{e,V=O}$ is the V=O stretching wavenumber corrected for anharmonicity and $\chi_{e,V=O}$ is the anharmonicity constant. By substituting the observed $\nu_{V=O,1\leftarrow0(R)}$ and $\nu_{V=O,2\leftarrow0(IR)}$ counterpart wavenumbers, the respective values for $\omega_{e,V=O}$ and $\chi_{e,V=O}$ are calculated and compiled in Table 2. Notably, the 6.3 × 10^{-3}–7.8 × 10^{-3} values calculated for χ_e are very reasonable[75] and justify the proposed mono-oxo configuration.

Significantly, a close inspection of the fundamental (~985–1025 cm^{-1}) and overtone (~1960–2035 cm^{-1}) V=O counterpart stretching regions of the Raman and FTIR spectra in Fig. 2 and 3 does not provide evidence for the occurrence of bands other than the already noted bands (I), (II) and double band (III). Moreover, the approximate doubling of the bands' distances in the FTIR overtone region does not reveal the presence of other bands that could arguably be assigned to the antisymmetric counterparts of bands (I) and (II), thereby corroborating the proposed mono-oxo termination configuration for Species-I and Species-II. Hence, to further strengthen the last statement, a peak analysis of the V=O stretching region is undertaken for the *in situ* Raman spectra and for the Raman spectra under forced dehydrated static equilibrium conditions obtained for the low-loaded 0.40VTiO$_2$(P25) and 0.74VTiO$_2$(P25) samples and the results are shown in Fig. 6. Notably, the TiO$_2$(P25) background is subtracted from the Raman spectra before undertaking the peak analysis. In all cases displayed in Fig. 6, a very satisfactory deconvolution is achieved that results in one single band for each of the Species-I and Species-II and two components for Species-III. Along the sequence of decreasing temperature, band (I) gains intensity at the expense of the intensity of band (II). The intensity of the double band feature (III) increases moderately upon lowering the temperature (430 → 175 °C) in the *in situ* Raman spectra (panels (A) and (C)), whilst it remains unchanged in the Raman spectra under forced dehydration static conditions (panels (B) and (D)). The occurrence of two components (of which the one at a higher wavenumber is more intense among the two) within the double band (III) in the stretching region below 1000 cm^{-1} implies the existence of a dioxo Species-III,

Table 2 Observed vibrational (Raman and FTIR) wavenumbers, vibrational isotope effects and anharmonicity parameters for VO$_x$ Species-I and Species-II for low coverage VO$_x$/TiO$_2$(P25) catalysts

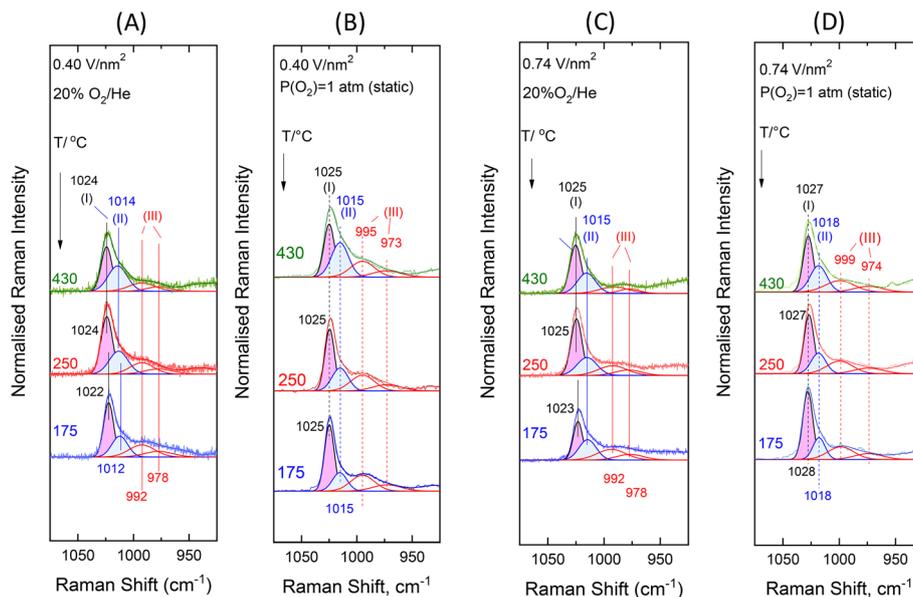| Species (V nm^{-2})	V=^{16}O				V=^{18}O	
	$\nu_{R, V=O, 1\leftarrow0}$	$\nu_{IR, V=O, 2\leftarrow0}$	$\omega_{e, V=O}$	$\chi_{e, V=O}$	Raman	Calculated[a]
Sp.-I (0.40)	1022	2031	1035	0.0063	978	978
Sp.-I (0.74)	1024	2034	1038	0.0068	980	980
Sp.-II (0.40)	1013	2010	1029	0.0078		
Sp.-II (0.74)	1014	2012	1030	0.0078		

[a] Based on the isotopic ratio of 1.0452.

Fig. 6 (A) and (C) Sequential (430 → 250 → 175 °C) *in situ* Raman spectra obtained under flowing 20% O_2/He at temperatures as indicated by each spectrum for VO_x/TiO$_2$(P25) with surface densities of (A) 0.40 V nm^{-2} and (C) 0.74 V nm^{-2}. Peak analysis is shown. The corresponding spectra obtained for TiO$_2$(P25) have been subtracted. (B) and (D) Sequential Raman spectra obtained at static equilibrium under $p_{O_2, 300 K}$ = 1 atm at temperatures as indicated by each spectrum for VO_x/TiO$_2$(P25) with surface densities of (B) 0.40 V nm^{-2} and (D) 0.74 V nm^{-2}. Peak analysis is shown. The corresponding spectra obtained for TiO$_2$(P25) have been subtracted. Spectral recording parameters: see the Fig. 2 caption.

of which the symmetric and antisymmetric modes are indeed expected to be separated by 10–30 cm^{-1}.[74]

3.1.4. Configuration and structural properties of dispersed VO_x sites. It has been demonstrated that a "completely dehydrated" $V^V O_x$/TiO$_2$ system is essentially an ideal approximation and would be stable at elevated temperatures only under high vacuum.[39,40] Hence, the term "hydroxylated" has been used to imply that H_2O is a ubiquitous molecule even under dehydrated feed conditions.[39,40] Models of progressive hydroxylation have indeed been validated both by experiment and theory. Molecular Dynamics (MD) and Density Functional Theory (DFT) studies[19,20,25] have shown that absolute dehydrated dispersed vanadia may exist only under the ideal conditions of complete absence of water. However, titania is known to retain water molecules that can be formed by con-

densation during the deposition of an oxo-metallic phase by titration of its surface hydroxyls.[28–31] A very well documented DFT study has recently shown that the configurations of dispersed VO_x sites on anatase are facet-dependent and that at low coverage (*i.e.* below 2 V nm^{-2}) a prevalent tetrahedral mono-oxo hydroxylated species occurs on the majority (101) facet and a less abundant octahedral-like mono-oxo hydroxylated species occurs on the minority (001) facet.[25] The results of the present work are in full alignment with the theoretically previewed scenario of the existence of distinct monomeric species, namely a majority mono-oxo monomeric tetrahedral-like Species-I with tetra-coordinated vanadium (CN$_V$ = 4) and a minority octahedral-like Species-II with penta-coordinated vanadium (CN$_V$ = 5). The proposed structural models for Species-I and Species-II are shown in Fig. 7. The terms "tetra-
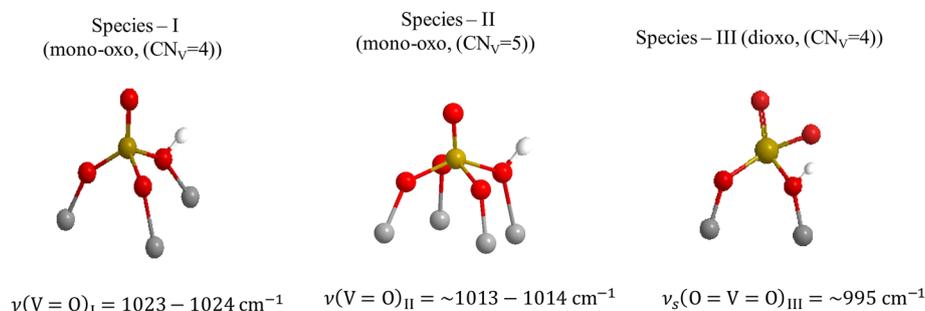

Species – I
(mono-oxo, (CN$_V$=4))

Species – II
(mono-oxo, (CN$_V$=5))

Species – III (dioxo, (CN$_V$=4))

$\nu(V=O)_I = 1023 - 1024$ cm^{-1}

$\nu(V=O)_{II} = \sim 1013 - 1014$ cm^{-1}

$\nu_s(O=V=O)_{III} = \sim 995$ cm^{-1}

Fig. 7 Plausible structural models, V coordination and termination/configuration characteristics for Species–I, Species–II and Species–III in mononuclear representations. Gold spheres, V; red spheres, O; grey spheres, Ti. H atoms (white spheres) are included to account for hydroxylation (see the text).

hedral-like with $CN_V = 4$" and "octahedral-like with $CN_V = 5$" are used to indicate that the proposed configurations are not perfect, in contrast they are distorted. The apparently contradictory "octahedral-like with $CN_V = 5$" term implies the occurrence of a sixth O atom situated on the titania support at an apical position *trans* to the terminal O atom and perpendicular to the distorted equatorial plane at a V–O distance that does not justify bonding (*e.g.* 2.6–2.8 Å).[25]

Species-I, VO$_4$H, possessing a distorted tetrahedral VO$_4$ configuration with one O atom offered by titania and a proton on a V–O–Ti bridge (bridge bond protonation, V–OH–Ti), comes out as the most stable V(v) species on the low coverage anatase (101) facet from DFT studies based on a Genetic Algorithm[76] using an unbiased approach.[25] Independently, DFT studies of the structure and stability of monomeric HVO$_x$ species on anatase[23] point to the same (Species-I) V(v) configuration as prevailing on anatase (101). A "Species-I" configuration on the anatase (101) facet has also been proposed very recently in periodic DFT calculations[77] combined with ^{51}V MAS NMR measurements on low coverage VO$_x$/TiO$_2$ catalysts that were in agreement with the nuclear shield and chemical shift evaluations for the VO$_4$H/"Species-I" cluster model. Species-I, representing a V(v) cluster, has also been considered in Molecular Dynamics calculations on the (001) anatase facet of vanadia–titania catalysts at low loadings.[19]

Hence, band (I) observed at 1023–1024 cm^{-1} in Fig. 2(A) and 3(A) and band (II) observed at ~1013 cm^{-1} are respectively assigned to the terminal stretching V=O modes of the tetrahedral-like Species-I with $CN_V = 4$, ν(V=O)$_I$, and octahedral-like Species-II with $CN_V = 5$, ν(V=O)$_{II}$. The higher wavenumber value for ν(V=O)$_I$ is justified by the lower coordination number for the V atom ($CN_V = 4$ *vs.* $CN_V = 5$). Interestingly, higher wavenumbers of 1025 and 1027 cm^{-1} are observed for ν(V=O)$_I$ for the low-loaded samples with 0.40 and 0.74 V nm^{-2} under forced dehydrated static equilibrium conditions (Fig. 2(C) and 3(C)), where a lower extent of hydroxylation prevails compared to the *in situ* conditions. The higher extent of hydroxylation prevailing under *in situ* conditions results in a downshift for the V=O terminal stretching wavenumber due to interactions with neighbouring hydroxyls, in agreement with the theoretical calculations of harmonic vibrational spectra.[19]

Structural changes upon cooling

The temperature-dependent features of the *in situ* Raman, *in situ* FTIR and static equilibrium Raman spectra (Fig. 2 and 3) are suggestive of structural transformations for the VO$_x$ species constituting the vanadia phase dispersed on TiO$_2$(P25). Water molecules retained by the titania surface get activated by lowering the temperature in the 430–175 °C range and mediate structural transformations. Experimental and theoretical (Molecular Dynamics and DFT) studies show that H$_2$O molecules, through dissociative adsorption, hydrolyse V–O–Ti bonds.[19,20,39] Hence, a progressive hydroxylation takes place by lowering the temperature. Additionally, DFT studies showed that at coverages below 0.8 V nm^{-2} where the titania

surface is more exposed, hydroxyl formation on the carrier is energetically favoured.[25] In contrast, above 1.7 V nm^{-2}, theoretical calculations suggest that having a surface hydroxyl is less stable compared to having a hydroxyl on a V–O–Ti site (*e.g.* V–O(H)–Ti).[25] Moreover, while molecular water adsorption is favored on "clean" (101) facets, dissociative H$_2$O adsorption is favoured near vacancies on defective (101) facets.[51]

To gain insight into the hydroxylation mechanisms, the spectral region of the surface hydroxyls is also explored. Fig. 8 portrays the temperature-dependence of the Raman spectra obtained under forced dehydrated static equilibrium for the low-loaded 0.40VTiO$_2$(P25) and 0.74VTiO$_2$(P25) samples in the spectral region of the OH groups. The corresponding Raman spectrum obtained for the TiO$_2$(P25) support under static equilibrium at 430 °C is included in each panel for comparison. Four bands due to surface hydroxyls are observed at 3710, 3675, 3640 and 3540 cm^{-1} for TiO$_2$(P25), in agreement with a recent report.[31] The spectra in Fig. 8 confirm that a progressive surface hydroxylation takes place upon lowering the temperature in the 430 → 250 → 175 °C sequence, thereby corroborating the aforementioned dissociative adsorption action of water.

The following observations can be made in Fig. 2 and 3 upon lowering the temperature in the sequence 430 → 250 → 175 °C: (a) the intensity of band (I) is increased at the expense of the intensity of band (II); (b) the band (III) doublet slightly gains intensity relative to band (I) under *in situ* conditions (Fig. 2 and 3, panels (A) and (B)). The pertinent structural transformations accounting for these temperature-dependent spectral changes are depicted in Fig. 9 (Schemes A and B). Namely (Fig. 9, Scheme A), by lowering the temperature, a water molecule gets activated and hydrolyses a V–O–Ti bond of Species-II, thereby resulting in the formation of Species-I plus
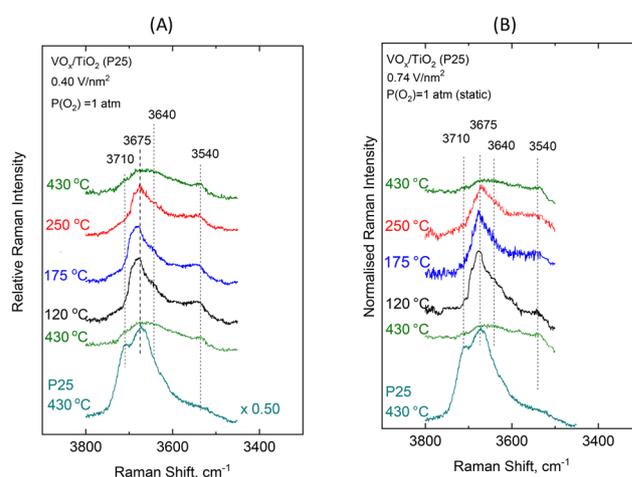

Fig. 8 VO$_x$/TiO$_2$(P25) with surface densities of (A) 0.40 V nm^{-2} and (B) 0.74 V nm^{-2}. Sequential (430 → 250 → 175 → 430 °C) Raman spectra at static equilibrium under $p_{O_2, 300 K} = 1$ atm at temperatures as indicated by each spectrum. Each panel includes the Raman spectrum of pure TiO$_2$(P25) at 430 °C as a reference. Spectral parameters: $\lambda_0 = 532.0$ nm; laser power, $w = 15$ mW; resolution, 2 cm^{-1}.
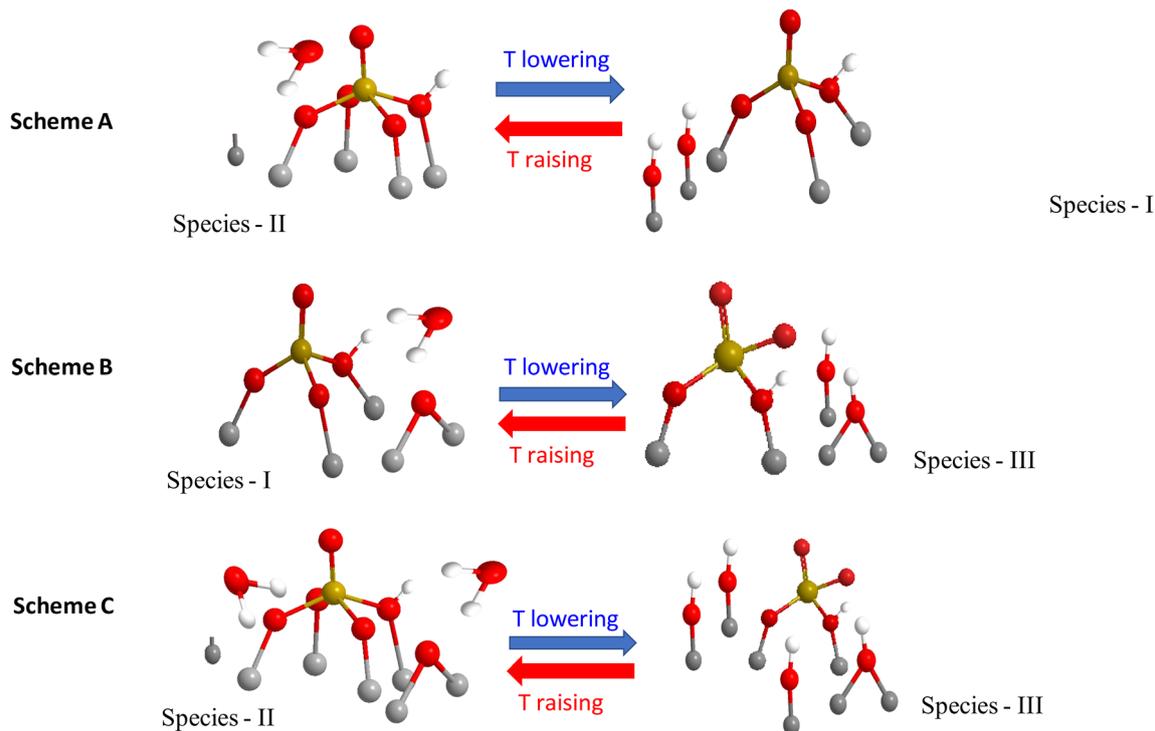
Fig. 9 Molecular level mechanisms of temperature-dependent reversible structural transformations. For simplicity, Species-I, Species-II and Species-III are shown in mononuclear representations. Scheme A: Species-II ↔ Species-I transformation mediated by one H_2O molecule; Scheme B: Species-I ↔ Species-III transformation mediated by one H_2O molecule; Scheme C: Species-II ↔ Species-III transformation mediated by two H_2O molecules, shown in one step.

two surface hydroxyls. Hence, band (II) is attenuated and band (I) gains intensity and appears sharper (Fig. 2, 3 and 6). Concomitantly, hydroxyl bands emerge in the respective spectral region (Fig. 8). Subsequent hydrolysing action on Species-I (favoured in the 250–175 °C range) results in the formation of Species-III plus two surface hydroxyls (Fig. 9, Scheme B). Importantly, as seen in Fig. 2, 3 and 8, upon heating up to 430 °C, the initial (*i.e.* before cooling) spectral features are fully reinstated, thereby evidencing that the observed structural changes are reversible. Moreover, no evidence limiting the observed effects was found when repeatedly cooling and heating the samples. Notably, the structural and configurational transformations shown in Fig. 9 are in full conformity with the corresponding temperature-dependent observations in Fig. 2, 3, 6 and 8.

Previously,[78] multiple V═O terminal stretching modes (at wavenumbers that are in agreement with the values reported in the present work, see *e.g.* Fig. 7) have been observed for VO$_x$/TiO$_2$(anatase, A), VO$_x$/TiO$_2$(rutile, R) and VO$_x$/TiO$_2$(brookite, B) catalysts, implying the occurrence of Species-I, Species-II and Species-III at varying proportions depending on the titania polymorph. Significantly, adopting the species notation of the present work, a larger extent of Species-II presence was found for VO$_x$/TiO$_2$(R) compared to VO$_x$/TiO$_2$(A). Interestingly, the extent of the presence of Species-II for VO$_x$/TiO$_2$(P25) in the present work (containing typically 80% anatase and 20% rutile) is graded as intermediate to the

corresponding states for VO$_x$/TiO$_2$(A) and VO$_x$/TiO$_2$(R) reported in ref. 78.

3.2. VO$_x$/TiO$_2$(P25) catalysts with intermediate and high coverage. Vibrational (Raman and FTIR) spectra and structural/configurational characteristics

At intermediate (*i.e.* 1.1 and 2.0 V nm^{-2}) and high (4.0 and 5.5 V nm^{-2}) coverage, the VO$_x$ sites constituting the dispersed vanadia phase also occur in associated configurations possessing V–O–V linkages resulting in increased (VO$_x$)$_n$ domain size. While surface hydroxyls with high basicity are titrated first in the initial deposition steps, hydroxyls of moderate basicity are also being titrated and come progressively into play as receptors of deposited VO$_x$ units with increasing coverage. Lower basicity for oxygen in a Ti–O–V anchoring site implies (according to the valence sum rule) a slightly stronger terminal stretching V═O bond and a commensurate blue shift for ν(V═O) with increasing coverage, as shown in Fig. 4. Moreover, an increase in the domain size induces a vibrational coupling mechanism between V–O– and V═O vibrations, thereby resulting in wavenumber shifts and intensity alterations for V═O modes.[79] Additionally, as discussed in the context of Fig. 4, the increase in coverage is connected with the emergence and gradual prominence of the very broad feature in the 915–930 cm^{-1} range ascribed to O–V–O and/or V–O–V functionalities. Hence, as shown in Fig. 10–13, the Raman spectra obtained for VO$_x$/TiO$_2$(P25) samples with cover-
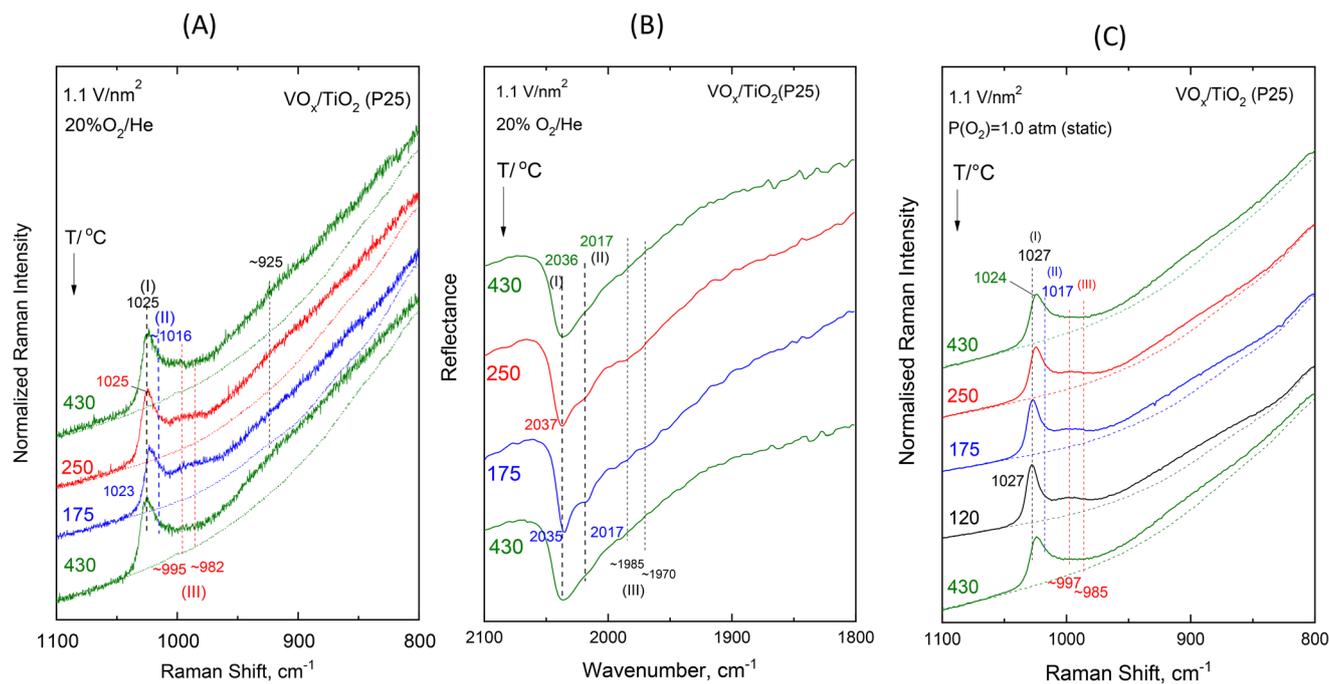
Fig. 10 $VO_x/TiO_2(P25)$ with a surface density of 1.1 V nm^{-2}: (A)–(C) see the caption to Fig. 2. Spectral recording parameters: see the Fig. 2 caption.

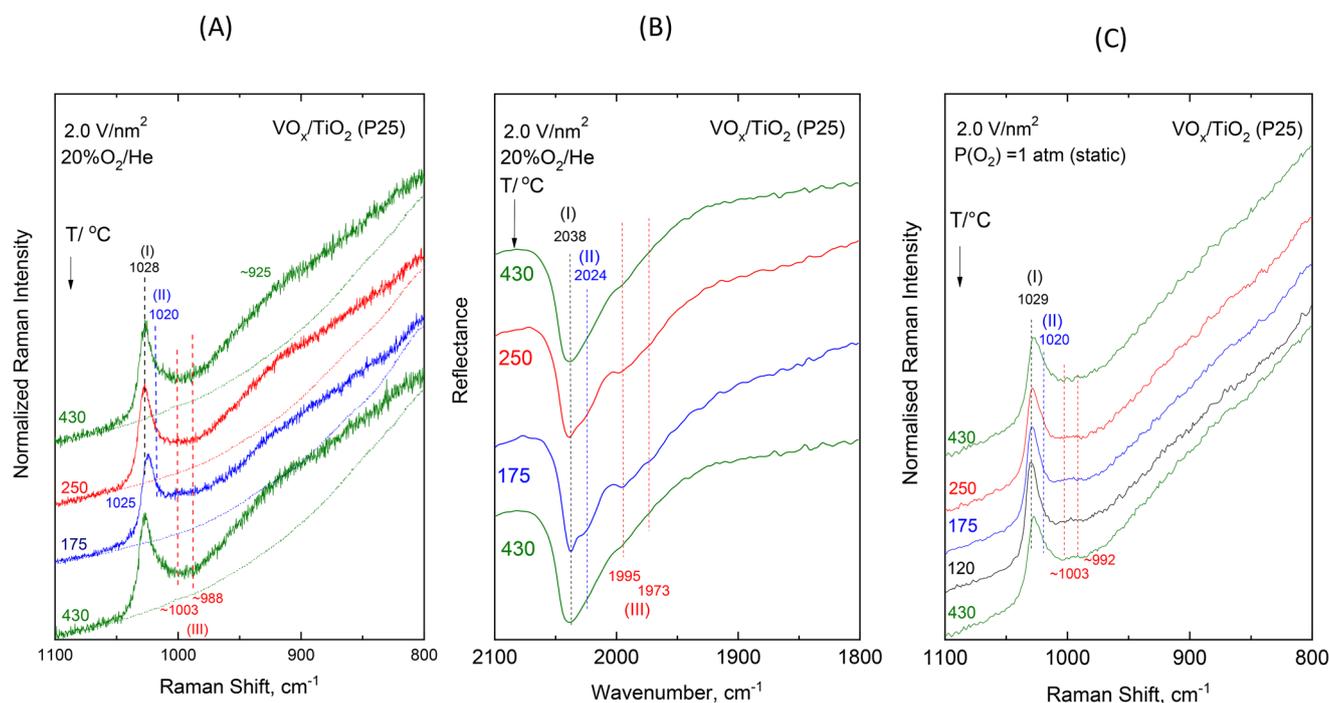**Fig. 11** $VO_x/TiO_2(P25)$ with a surface density of 2.0 V nm^{-2}: (A)–(C) see the caption to Fig. 2. Spectral recording parameters: see the Fig. 2 caption.

age in the 1.1–5.5 V nm^{-2} range exhibit broad continua without perceptive components that tend to prevail with increasing coverage. In particular, for samples with high coverage (*i.e.* 4.0 and 5.5 V nm^{-2}) the broad feature centred at ~930 cm^{-1} (Fig. 12(A) and 13(A)) obscures the region of band (III) and significantly perturbs the band shapes in the V=O stretching region of bands (I) and (II). In contrast, the counterpart *in situ* FTIR spectra do not display any features in the respective overtone 1800–1850 cm^{-1} region, thereby indicating that the O–V–O and/or V–O–V modes are infrared silent.

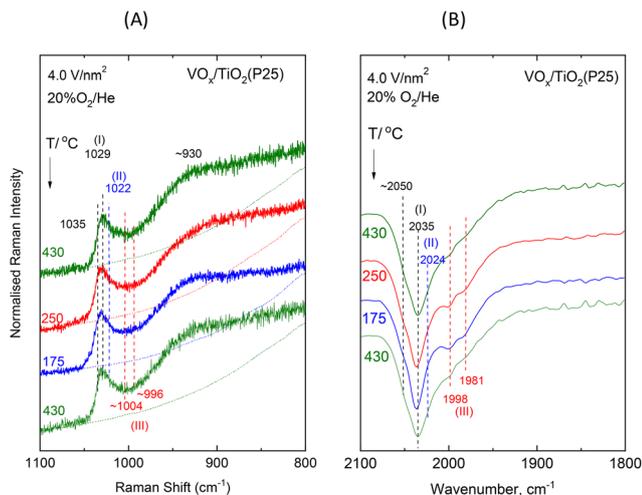**Fig. 12** VOₓ/TiO₂(P25) with a surface density of 4.0 V nm⁻²: (A) and (B) see the caption to Fig. 2. Spectral recording parameters: see the Fig. 2 caption.

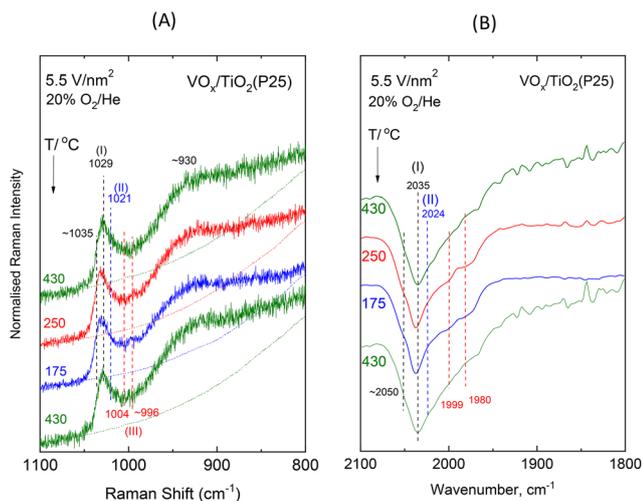**Fig. 13** VOₓ/TiO₂(P25) with a surface density of 5.5 V nm⁻²: (A) and (B) see the caption to Fig. 2. Spectral recording parameters: see the Fig. 2 caption.

Consequently, the overtone components of the double band (III) are clearly discerned in the pertinent *in situ* FTIR spectra.

Interestingly, the reversible temperature-dependent structural/configurational transformations pertaining to Species-I, Species-II and Species-III established for samples with low coverages of 0.40 and 0.74 V nm⁻² are also evidenced for intermediate and high coverage from the Raman and FTIR spectra shown in Fig. 10–13, without any spectral evidence in contrast. Namely, when the temperature is lowered in the sequence 430 → 250 → 175 °C, the vibrational spectra obtained for 1.1VTiO₂(P25) and 2.0VTiO₂(P25) under *in situ* (Raman and FTIR, Fig. 10(A), (B) and 11(A), (B)) and static equilibrium (Raman, Fig. 10(C) and (C)) conditions invariably show that band (I) initially gains intensity at the relative expense of band (II) and band (III) is relatively strengthened in the lower temp-

erature region. For samples with coverages of 4.0 and 5.5 V nm⁻², while the *in situ* Raman spectra (Fig. 12(A) and 13(A)) are dominated by the broad continuum centered at ∼930 cm⁻¹ ascribed to O–V–O and V–O–V modes, the *in situ* FTIR spectra in the overtone region clearly show the aforementioned identified band intensity changes that follow the lowering of the temperature. Worth mentioning is also the observation of a shoulder component at the high wavenumber wing of band (I) in the Raman and FTIR spectra obtained for samples with high coverage (at *ca.* 1035 and 2045 cm⁻¹, respectively, Fig. 12 and 13), which is attributed to the vibrational coupling between V–O– and V=O bonds (*vide ante*). Significantly, the spectral changes taking place when cooling the samples in the 430 → 250 → 175 °C sequence are fully reversible, *i.e.* when reheating the samples to 430 °C, the catalyst molecular structure is reinstated and the initial spectrum at 430 °C is reproduced in each case (see Fig. 10–13).

Hence, although multiple association steps may have resulted in two-dimensional polymeric (VOₓ)ₙ domains at intermediate and high coverage, it turns out that Species-I, Species-II and Species-III constitute the basic building units of the dispersed vanadia phase by maintaining their principal configurational characteristics (*i.e.* coordination number of the V atom and termination configuration).

3.3. Implications for reactivity and catalysis

Numerous theoretical and experimental investigations have focused on key fundamental mechanistic aspects and/or attempted to identify active sites and reveal their roles in catalytic reactions involving vanadia–titania catalysts. Importantly, many questions remain open, in part due to the complexity of the structural characterisation of the dispersed vanadia phase. The aim of the present work was an in-depth characterisation of the molecular structure of the (VOₓ)ₙ phase dispersed on titania (P25). Hence, one cannot directly propose new insight or suggestions for revealing the mechanisms in catalytic reactions involving VOₓ/TiO₂ catalysts. However, significant new insight is gained into the structural characterization of the VOₓ sites constituting the vanadia phase dispersed on titania. Determining which of the species present constitute the *active* phase remains a formidable challenge, given that several species may be present as spectators and that the majority of species are not necessarily the active sites. A discussion on reactivity issues can, however, be provided.

With reference, *e.g.* to the NH₃–SCR of NOₓ *i.e.* the widest application of vanadia–titania catalysts, it is well established that higher SCR activity is obtained at high vanadia coverage where polymeric species prevail and V centers occur at adjacent sites. However, approaching the integral catalyst function through understanding the catalytic behaviour of mononuclear VOₓ sites has also gained focused attention.[80–82]

The results of the present investigation show that at low coverage (*i.e.* <1 V nm⁻²) isolated VOₓ sites occur in the form of three distinct configurations: (a) Species-I, of mono-oxo distorted tetrahedral-like arrangement with CN_V = 4; (b) Species-II, of mono-oxo distorted octahedral-like arrangement with

$CN_V = 5$; and (c) Species-III, of di-oxo arrangement with $CN_V = 4$. Interestingly, the results obtained for coverages in the 1.1–5.5 V nm^{-2} range show that the polymeric dispersed vanadia phase consists of building units possessing the characteristics of Species-I, Species-II and Species-III.

A consensus on a number of redox processes is that among the three types of V–O bonds (terminal V=O, anchoring V–O–Ti and bridging V–O–V) the anchoring V–O–Ti site prevails as governing the catalytic performance. In the past, the relevance between V=O sites and the catalytic activity of titania-supported vanadia had been claimed for *o*-xylene oxidation,[83] whilst subsequently controverted[15] when evidence was provided that V–O–support functionalities are the active sites for hydrocarbon oxidation reactions.

Significantly, theoretical (DFT) and experimental (EPR) investigations[25] have shown that the VO$_x$ site involved in the redox SCR mechanistic cycle maintains its V=O termination with V changing between the +5 and +4 oxidation states.[73] Moreover, the reactivity of Ti–O–V sites is linked to the catalytic activity because the reduction step was found to involve adjacent Ti–O–V sites.[80]

Studies[10,16,84–86] on methanol and alkane ODH processes also showed V=O bond stability and ruled out the participation of V=O in pertinent reaction pathways. Additionally, focusing on the ethanol ODH, the oxygen on the V–O–V bridging sites has been shown to be irrelevant to the intrinsic catalytic activity, suggesting that the presence of these functionalities is not a controlling factor for partial oxidation processes.[87] On the other hand, the claim that the oxygen associated with the V–O-support site is the critical site for a number of ODH processes is sustained.[85,88]

The present work underlines the promoting role of the V–O–Ti functionalities in the species transformation mechanism (reactivity to retained surface water), when the V=O bond appears unreactive at high temperature under dehydrated feed conditions and forced dehydrated conditions. The argument for the V=O bond stability is further strengthened by the slower ^{18}O/^{16}O isotopic substitution of the terminal oxygen site compared to the one on the V–O–Ti linkages (see Fig. 5(A) and (B)). The last is affirmed by the slight red shift of the V=^{16}O mode during the first ^{18}O/^{16}O exchange cycles, which indicates that the initiation of the isotope exchange takes place on the V–O–Ti linkages followed by a subsequent ^{18}O substitution on the V=^{16}O sites, according to the next-nearest-neighbor vibrational isotope effect.[31,57,59]

The present work provides clear evidence that the dispersed vanadia phase is heterogeneous and that among the structural units dispersed in titania Species-II (*i.e.* the mono-oxo distorted octahedral-like unit which is proposed to exist in (001) facets[25]), although being a minority species, it has the highest reactivity to water molecules that are retained on the surface and become activated when lowering the temperature (*vide ante*). The V–O–Ti sites of Species-II are hydrolysed with higher priority upon cooling from 430 to 250 °C, thereby implying different reactivity of the anchoring V–O–Ti functionalities of Species-I and Species-II.

Previous studies[85,89] on the activity of supported vanadia catalysts in alkane ODH and methanol ODH processes had also focused on the relationship between the activity and the electronegativity of the support cation by investigating different supports and exploring pertinent support effects on structure–activity relationships.[90] It has been suggested that low support cation electronegativity implies higher reactivity of oxygen along V–O-support linkages in the redox processes investigated.

In synopsis, while the implication of the present work on catalysis is by nature indirect, insights into the structural properties of the dispersed VO$_x$ phase and into the reactivity of V–O–Ti sites could contribute to the discussion on structure–function relationships for several catalytic processes benefited by titania-supported vanadia catalysts.

4. Conclusions

In synopsis, molecular vibrational spectroscopy is used to achieve progress in the characterisation of the molecular structure and configuration of VO$_x$ sites dispersed on TiO$_2$(P25). *In situ* (Raman and FTIR) spectroscopies (the former complemented also by ^{18}O/^{16}O isotope exchange) under dehydrated feed conditions as well as static equilibrium Raman spectroscopy under forced dehydrated conditions are exploited. The dispersed vanadia phase is found to be heterogeneous, constituted of three distinct VO$_x$ species/units, of which the relative presence is found to be temperature-dependent. Species-I with a mono-oxo distorted tetrahedral configuration ($CN_V = 4$) is the majority species. Species-II with a mono-oxo distorted octahedral configuration ($CN_V = 5$) and Species-III with a di-oxo configuration are the minority species. When lowering the temperature from 430 to 250 °C, water molecules retained by the surface mediate reversible structural transformations according to Species-II → Species-I and with further lowering (from 250 to 175 °C) according to Species-I → Species-III. The mechanism of the structural transformations is the hydrolysis of the V–O–Ti sites resulting in hydroxylation as evidenced also by the Raman spectra obtained in the hydroxyl region. Species-II with a mono-oxo distorted octahedral ($CN_V = 5$) configuration exhibits the highest reactivity.

For low coverages (up to 0.74 V nm^{-2}), the dispersed vanadia phase consists almost exclusively of isolated (monomeric) VO$_x$ sites (Species-I, Species-II, Species-III). Whereas for coverages above 1 V nm^{-2} a gradual polymerization takes place through V–O–V linkages, the basic geometric characteristics of the VO$_x$ building units constituting the (VO$_x$)$_n$ polymeric domains maintain the configurations of Species-I, Species-II, and Species-III.

Different extents of hydroxylation are evidenced when comparing the results obtained under *in situ* dehydrated feed conditions and static equilibrium forced dehydrated conditions. The forced dehydration procedure preceding the sample preparation for the Raman study under static equilibrium limits the temperature-dependent structural transformation effects due

to the higher extent of dehydration achieved, also confirmed by a slightly higher wavenumber for the $\nu_{V=O}$ mode. The present study confirms that the fully dehydrated state for dispersed vanadia is only an ideal approximation occurring possibly only in the complete absence of water (*e.g.* under vacuum). The results contribute to a close focus on insight that improves the understanding of the molecular structure of the VO_x phase dispersed on titania.

Conflicts of interest

There are no conflicts to declare.

References

1 I. E. Wachs, Recent conceptual advances in the catalysis science of mixed metal oxide catalytic materials, *Catal. Today*, 2005, **100**, 79–94.

2 L. Artiglia, S. Agnoli and G. Granozzi, Vanadium Oxide Nanostructures on Another Oxide: The Viewpoint from Model Catalysts Studies, *Coord. Chem. Rev.*, 2015, **301–302**, 106–122.

3 P. Gabrielsson and H. G. Pedersen, in *Handbook of Heterogeneous Catalysis*, ed. G. Ertl, H. Knözinger, F. Schüth and J. Weitkamp, Wiley-VCH, Weinheim, 2008.

4 J. Shen and C. Hess, High Surface Area $VO_x/TiO_2/SBA-15$ Model Catalysts for Ammonia SCR Prepared by Atomic Layer Deposition, *Catalysts*, 2020, **10**, 1386.

5 C. Hess, P. Waleska, M. Ratzka, T. V. W. Janssens, S. B. Rasmussen and P. Beato, Hierarchical Vanadia Model Catalysts for Ammonia Selective Catalytic Reduction, *Top. Catal.*, 2017, **60**, 1631–1640.

6 J.-K. Lai and I. E. Wachs, A Perspective on the Selective Catalytic Reduction (SCR) of NO with NH_3 by Supported V_2O_5–WO_3/TiO_2 Catalysts, *ACS Catal.*, 2018, **8**, 6537–6551.

7 I. Giakoumelou, Ch. Fountzoula, Ch. Kordulis and S. Boghosian, Molecular structure and catalytic activity of V_2O_5/TiO_2 catalysts for the SCR of NO by NH_3: In situ Raman spectra in the presence of O_2, NH_3, NO, H_2, H_2O and SO_2, *J. Catal.*, 2006, **239**, 1–12.

8 M. M. Koranne, J. G. Goodwin and G. Marcelin, Partial Oxidation of Methane over Silica-Supported and Alumina-supported Vanadia Catalysts, *J. Catal.*, 1994, **148**, 388–391.

9 G. Deo and I. E. Wachs, Reactivity of Supported Vanadium-oxide Catalysts – the Partial Oxidation of Methanol, *J. Catal.*, 1994, **146**, 323–334.

10 A. Christodoulakis, M. Machli, A. A. Lemonidou and S. Boghosian, Molecular Structure and Reactivity of Vanadia Based Catalysts for Propane Oxidative Dehydrogenation Studied by *in situ* Raman Spectroscopy and Catalytic Activity Measurements, *J. Catal.*, 2004, **222**, 293–306.

11 W. D. Harding, K. E. Birkeland and H. H. Kung, Selective Oxidation of Butane on Phosphorous-Modified Silica-Supported Vanadia Catalysts, *Catal. Lett.*, 1994, **28**, 1–7.

12 M. Ek, L. Arnarson, P. G. Moses, S. B. Rasmussen, M. Skoglundh, E. Olsson and S. Helveg, Probing Surface-sensitive Redox Properties of VO_x/TiO_2 catalyst nanoparticles, *Nanoscale*, 2021, **13**, 7266–7272.

13 S. S. R. Putluru, L. Schill, A. Godiksen, R. Poreddy, S. Mossin, A. D. Jensen and R. Fehrmann, Promoted V_2O_5/TiO_2 Catalysts for Selective Catalytic Reduction of NO with NH_3 at Low Temperatures, *Appl. Catal., B*, 2016, **183**, 282–290.

14 M. Zhu, J. K. Lai, U. Tumuluri, M. E. Ford, Z. Wu and I. E. Wachs, Reaction Pathways and Kinetics for Selective Catalytic Reduction (SCR) of Acidic NO_x Emissions from Power Plants with NH_3, *ACS Catal.*, 2017, **7**, 8358–8361.

15 I. E. Wachs and B. M. Weckhuysen, Structure and Reactivity of Surface Vanadium Oxide Species on Oxide Supports, *Appl. Catal., A*, 1997, **157**, 67–90.

16 B. M. Weckhuysen and D. E. Keller, Chemistry, Spectroscopy and the Role of Supported Vanadium Oxides in Heterogeneous Catalysis, *Catal. Today*, 2003, **78**, 25–46.

17 N. Y. Topsøe, M. Anstrom and L. A. Dumesic, Raman, FTIR and Theoretical Evidence for Dynamic Structural Rearrangements of Vanadia/titania DeNO$_x$ Catalysts, *Catal. Lett.*, 2001, **76**, 11–20.

18 L. Lietti, J. Svachula, P. Forzatti, G. Busca, G. Ramis and P. Bregani, Surface and Catalytic Properties of Vanadia-Titania and TungstaTitania Systems in the Selective Catalytic Reduction of Nitrogen Oxides, *Catal. Today*, 1993, **17**, 131–139.

19 A. E. Lewandowska, M. Calatayud, F. Tielens and M. A. Bañares, Dynamics of Hydration in Vanadia–Titania Catalysts at Low Loading: A Theoretical and Experimental Study, *J. Phys. Chem. C*, 2011, **115**, 24133–24142.

20 A. E. Lewandowska, M. Calatayud, F. Tielens and M. A. Bañares, Hydration Dynamics for Vanadia/Titania Catalysts at High Loading: A Combined Theoretical and Experimental Study, *J. Phys. Chem. C*, 2013, **117**, 25535–25544.

21 G. T. Went, L.-J. Leu and A. T. Bell, Quantitative Structural Analysis of Dispersed Vanadia Species in TiO_2(Anatase)-Supported V_2O_5, *J. Catal.*, 1992, **134**, 479–491.

22 M. Calatayud, B. Mguig and C. A. Minot, Periodic Model for the V_2O_5–TiO_2 (anatase) Catalyst. Stability of Dimeric Species, *Surf. Sci.*, 2003, **526**, 297–308.

23 Y.-J. Du, Z. Hua Li and K.-N. Fan, Periodic density functional theory studies of the VO_x/TiO_2 (anatase) catalysts: Structure and stability of monomeric species, *Surf. Sci.*, 2012, **606**, 956–964.

24 A. Vittadini and A. Selloni, Periodic Density Functional Theory Studies of Vanadia - Titania Catalysts: Structure and Stability of the Oxidized Monolayer, *J. Phys. Chem. B*, 2004, **108**, 7337–7343.

25 L. Arnarson, S. B. Rasmussen, H. Falsig, J. V. Lauritsen and P. G. Moses, Coexistence of Square Pyramidal Structures of

Oxo Vanadium (+5) and (+4) Species Over Low-Coverage VO_x/TiO_2 (101) and (001) Anatase Catalysts, *J. Phys. Chem. C*, 2015, **119**, 23445–23452.

26 J. Strunk, M. A. Banares and I. E. Wachs, Vibrational Spectroscopy of Oxide Overlayers, *Top. Catal.*, 2017, **60**, 1577–1617.

27 M. A. Vuurman, I. E. Wachs and A. M. Hirt, Structural Determination of Supported V_2O_5-WO_3/TiO_2 Catalysts by in situ Raman Spectroscopy and X-ray Photoelectron Spectroscopy, *J. Phys. Chem.*, 1991, **95**, 9928–9937.

28 C. Andriopoulou and S. Boghosian, Molecular Structure and Termination Configuration of Oxo-Re(VII) Catalyst Sites Supported on Titania, *Catal. Today*, 2020, **355**, 665–677.

29 C. Andriopoulou and S. Boghosian, Heterogeneity of Deposited Phases in Supported Transition Metal Oxide Catalysts: Reversible Temperature-Dependent Evolution of Molecular Structures and Configurations, *Phys. Chem. Chem. Phys.*, 2018, **20**, 1742–1751.

30 C. Andriopoulou and S. Boghosian, Tuning the Configuration of Dispersed Oxometallic Sites in Supported Transition Metal Oxide Catalysts: A Temperature Dependent Raman Study, *Catal. Today*, 2019, **336**, 74–83.

31 Th. Kentri, A. Trimpalis, A. Misa, E. Kordouli, Th. Ramantani and S. Boghosian, Rethinking Molecular Structures of $W^{VI}O_x$ Sites Dispersed on Titania. Distinct Mono-Oxo Configurations at 430 °C and Temperature-Dependent Transformations, *Dalton Trans.*, 2022, **51**, 7455–7475.

32 J. P. Thielemann and C. Hess, Monitoring Silica Supported Molybdenum Oxide Catalysts at Work: A Raman Spectroscopic Study, *ChemPhysChem*, 2013, **14**, 441–447.

33 S. Eibl, B. C. Gates and H. Knozinger, Structure of WO_x/TiO_2 Catalysts Prepared from Hydrous Titanium Oxide Hydroxide: Influence of Preparation Parameters, *Langmuir*, 2001, **17**, 107–115.

34 A. Yoboue, A. Susset, A. Tougerti, D. Gallego, S. V. Ramani, M. Kalyanikar, D. S. Dolzhnikov, S. G. Wubshet, Y. Wang, S. Cristol, V. Briois, C. La Fontaine, R. M. Gauvin, J.-F. Paul and E. Berier, An Easily Accessible Re-Based Catalyst for The Selective Conversion of Methanol: Evidence for an Unprecedented Active Site Structure Through Combined Operando Techniques, *Chem. Commun.*, 2011, **47**, 4285–4287.

35 K. Ding, A. Gulec, A. M. Johnson, T. L. Drake, W. Wu, Y. Lin, E. Weitz, L. D. Marks and P. C. Stair, Highly Efficient Activation, Regeneration, and Active Site Identification of Oxide-Based Olefin Metathesis Catalysts, *ACS Catal.*, 2016, **6**, 5740–5746.

36 S. Lwin and I. E. Wachs, Olefin Metathesis by Supported Metal Oxide Catalysts, *ACS Catal.*, 2014, **4**, 2505–2520.

37 B. MacQueen, B. Ruiz-Yi, M. Royko, A. Heyden, Y. J. Pagan-Torres, C. Williams and J. Lauterbach, *In situ* Oxygen Isotopic Exchange Vibrational Spectroscopy of Rhenium Oxide Surface Structures on Cerium Oxide, *J. Phys. Chem. C*, 2020, **124**, 7174–7181.

38 S. Lwin, C. Keturakis, J. Handzlik, P. Sautet, Y. Li, A. I. Frenkel and I. E. Wachs, Surface ReO_x Sites on Al_2O_3 and Their Molecular Structure–Reactivity Relationships for Olefin Metathesis, *ACS Catal.*, 2015, **5**, 1432–1444.

39 S. B. Rasmussen, R. Portela, P. Bazin, P. Ávila, M. A. Bañares and M. Daturi, Transient Operando Study on The NH_3/NH^{4+} Interplay in V-SCR Monolithic Catalysts, *Appl. Catal., B*, 2018, **224**, 109–115.

40 M. O. Guerrero-Perez, M. V. Martinez-Huerta and M. A. Bañares, Molecularly Dispersed Vanadium Oxide: Structure–Reactivity Relationships for Reducibility and Hydrocarbon Oxidation, in *Catalysis Series No. 41, Vanadium Catalysis*, ed. M. Sutradhar, J. A. L. da Silva and A. J. L. Pombeiro, Royal Society of Chemistry, 2021, ch. 13, pp. 321–339.

41 E. Tella, A. Trimpalis, A. Tsevis, Ch. Kordulis, A. Lycourghiotis, S. Boghosian and K. Bourikas, Advanced Synthesis and Characterization of Vanadia/Titania Catalysts Through a Molecular Approach, *Catalysts*, 2021, **11**, 322.

42 Q. Shi, Y. Li, Y. Zhou, S. Miao, N. Ta, E. Zhan, J. Liu and W. Shen, The Shape Effect of TiO_2 in VO_x/TiO_2 Catalysts for Selective Reduction of NO by NH_3, *J. Mater. Chem. A*, 2015, **3**, 14409–14415.

43 W.-Z. Li, F. Gao, Y. Li, E. D. Walter, J. Liu, C. H. F. Peden and Y. Wang, Nanocrystalline Anatase Titania-Supported Vanadia Catalysts: Facet-Dependent Structure of Vanadia, *J. Phys. Chem. C*, 2015, **119**, 15094–15102.

44 M. Sanati, L. R. Wallenberg, A. Andersson, S. Jansen and Y. Tu, Vanadia Catalysts on Anatase, Rutile, and TiO_2(B) for the Ammoxidation of Toluene: an ESR and High-Resolution Electron Microscopy Characterization, *J. Catal.*, 1991, **132**, 128–144.

45 M. Li and E. I. Altman, Reactivity of Epitaxial Vanadia on TiO_2: Are Support Interactions Required for Reactivity?, *J. Phys. Chem. C*, 2009, **113**, 2798–2805.

46 G. Centi, Nature of Active Layer in Vanadium Oxide Supported on Titanium Oxide and Control of its Reactivity in the Selective Oxidation and Ammoxidation of Alkylaromatics, *Appl. Catal., A*, 1996, **147**, 267–298.

47 M. Ek, Q. M. Ramasse, L. Arnarson, P. G. Moses and S. Helveg, Visualizing atomic-scale redox dynamics in vanadium oxide-based catalysts, *Nat. Commun.*, 2017, **8**, 305–313.

48 G. Busca, Differentiation of Mono-oxo and Polyoxo and of Monomeric and Polymeric Vanadate, Molybdate and Tungstate Species in Metal Oxide Catalysts by IR and Raman Spectroscopy, *J. Raman Spectrosc.*, 2002, **33**, 348–358.

49 M. A. Banares and I. E. Wachs, Molecular Structures of Supported Metal Oxide Catalysts Under Different Environments, *J. Raman Spectrosc.*, 2002, **33**, 359–380.

50 C. Hess, In Situ Raman Spectroscopy of Catalysts: Examples from Current Research, *Top. Catal.*, 2013, **56**, 1593–1600.

51 G. D. Panagiotou, T. Petsi, K. Bourikas, C. S. Garoufalis, A. Tsevis, N. Spanos, C. Kordulis and A. Lycourghiotis, Mapping the Surface (Hydr)oxo-groups of Titanium Oxide and its Interface with an Aqueous Solution: the Stae of the Art and a New Approach, *Adv. Colloid Interface Sci.*, 2008, **142**, 20–42.

52 F. Xiong, L.-L. Yin, F. Li, Z. Wu, Z. Wang, G. Sun, H. Xu, P. Chai, X.-Q. Gong and W. Huang, Anatase TiO$_2$(001)-(1 × 4) Surface is Intrinsically More Photocatalytically Active than the Rutile TiO$_2$(110)-(1 × 1) Surface, *J. Phys. Chem. C*, 2019, **123**, 24558–24565.

53 K. Bourikas, C. Kordulis and A. Lycourghiotis, The Role of The Liquid—Solid Interface in The Preparation of Supported Catalysts, *Catal. Rev. Sci. Eng.*, 2006, **48**, 363–444.

54 B. Ohtani, O. O. Prieto-Mahaney, D. Li and R. Abe, What is Degussa(Evonik) P25? Crystalline composition analysis, reconstruction from isolated pure particlesand photo-catalytic activity test, *J. Photochem. Photobiol., A*, 2010, **216**, 179–182.

55 A. Tribalis, G. D. Panagiotou, G. Tsilomelekis, A. G. Kalampounias, K. Bourikas, C. Kordulis, S. Boghosian and A. Lycourghiotis, Temperature-Dependent Evolution of The Molecular Configuration of Oxo-Tungsten(VI) Species Deposited on the Surface of Titania, *J. Phys. Chem. C*, 2014, **118**, 11319–11332.

56 A. Christodoulakis and S. Boghosian, Molecular Structure and Activity of Molybdena Catalysts Supported on Zirconia for Ethane Oxidative Dehydrogenation Studied by Operando Raman Spectroscopy, *J. Catal.*, 2008, **260**, 178–187.

57 G. Tsilomelekis and S. Boghosian, On the Configuration, Molecular Structure and Vibrational Properties of MoO$_x$ Sites on Alumina, Zirconia, Titania and Silica, *Catal. Sci. Technol.*, 2013, **3**, 1869–1888.

58 C. Andriopoulou, D. Harris, H. Stephenson, A. M. Eftsathiou and S. Boghosian, In situ Raman Spectroscopy as a Tool for Discerning Subtle Structural Differences Between Commercial (Ce,Zr)O$_2$-Based OSC Materials of Identical Composition, *Catalysts*, 2020, **10**, 462.

59 G. Tsilomelekis and S. Boghosian, In Situ Raman and FTIR Spectroscopy of Molybdenum(VI) Oxide Supported on Titania Combined with ^{18}O/^{16}O Exchange: Molecular Structure, Vibrational Properties and Vibrational Isotope Effects, *J. Phys. Chem. C*, 2011, **118**, 2146–2154.

60 G. Tsilomelekis and S. Boghosian, Structural and Vibrational Properties of Molybdena Catalysts Supported on Alumina and Zirconia Studied by in Situ Raman and FTIR Spectroscopies Combined with ^{18}O/^{16}O Isotopic Substitution, *Catal. Today*, 2010, **158**, 146–155.

61 S. Boghosian, Vibrational Modes and Structure of Vanadium(V) Complexes in M$_2$SO$_4$-V$_2$O$_5$ (M = K, Cs) Molten Salt Mixtures, *J. Chem. Soc., Faraday Trans.*, 1998, **94**, 3463–3469.

62 S. Boghosian, A. Chrissanthopoulos and R. Fehrmann, Structure of Vanadium Oxosulfato Complexes in V$_2$O$_5$-

M$_2$S$_2$O$_7$-M$_2$SO$_4$ (M=K, Cs) Melts. A High Temperature Spectroscopic Study, *J. Phys. Chem. B*, 2002, **106**, 49–56.

63 A. G. Kalampounias and S. Boghosian, Distribution of Tellurite Polymorphs in the xM$_2$O–(1−x)TeO$_2$ (M = Li, Na, K, Cs, and Rb) Binary Glasses Using Raman Spectroscopy, *Vib. Spectrosc.*, 2012, **59**, 18–22.

64 I. E. Wachs, G. Deo, B. M. Weckhhuysen, A. Andreini, M. A. Vuurman, M. de Boer and M. D. Amiridis, Selective Catalytic Reduction of NO with NH$_3$ over Supported Vanadia Catalysts, *J. Catal.*, 1996, **161**, 211–221.

65 G. T. Went, S. T. Oyama and A. T. Bell, Laser Raman Spectroscopy of Supported Vanadium Oxide Catalysts, *J. Phys. Chem.*, 1990, **94**, 4240–4246.

66 J. P. Dunn, P. R. Koppula, H. G. Stenger and I. E. Wachs, Oxidation of Sulfur Dioxide to Sulfur Trioxide over Supported Vanadia Catalysts, *Appl. Catal., B*, 1998, **19**, 103–117.

67 G. T. Went, L.-J. Leu and A. T. Bell, Quantitative Structural Analysis of Dispersed Vanadia in TiO$_2$(Anatase) – Supported V$_2$O$_5$, *J. Catal.*, 1992, **134**, 479–491.

68 Z. Wu, S. Dai and S. H. Overburry, Multiwavelength Raman Spectroscopic Study of Silica-Supported Vanadium Oxide Catalysts, *J. Phys. Chem. C*, 2010, **114**, 412–422.

69 J.-M. Jehng, G. Deo, B. M. Weckhuysen and I. E. Wachs, Effect of Water Vapor on the Molecular Structures of Supported Vanadium Oxide Catalysts at Elevated Temperatures, *J. Mol. Catal. A: Chem.*, 1996, **110**, 41–54.

70 B. M. Weckhuysen, J.-M. Jehng and I. E. Wachs, In Situ Raman Spectroscopy of Supported Transition Metal Oxide Catalysts: ^{18}O$_2$-^{16}O$_2$ Isotopic Labeling Studies, *J. Phys. Chem. B*, 2000, **104**, 7382–7387.

71 L. J. Burcham, G. Deo, X. Gao and I. E. Wachs, In situ IR, Raman, and UV-Vis DRS Spectroscopy of Supported Vanadium Oxide Catalysts During Methanol Oxidation, *Top. Catal.*, 2000, **11–12**, 85–100.

72 M. Zhu, J.-K. Lai, U. Tumuluri, Z. Wu and I. E. Wachs, Nature of Active Sites and Surface Intermediates During SCR of NO with NH$_3$ by Supported V$_2$O$_5$ –WO$_3$/TiO$_2$ Catalysts, *J. Am. Chem. Soc.*, 2017, **139**, 15624–15627.

73 A. L. Godiksen and S. B. Rasmussen, Identifying the Presence of [V=O]$^{2+}$ During SCR Using *in situ* Raman and UV Vis Spectroscopy, *Catal. Today*, 2019, **336**, 45–49.

74 K. Nakamoto, *Infrared and Raman Spectra of Inorganic and Coordination Compounds*, Wiley – Interscience, New York, 6th edn, 2009.

75 G. Herzberg, *Molecular Spectra and Molecular Structure, I, Spectra of Diatomic Molecules*, Van Nostrand Company Inc., Princeton, 2nd edn, 1950.

76 L. B. Vilhelmsen and B. Hammer, A Genetic Algorithm for First Principles Global Structure Optimization of Supported Nano Structures, *J. Chem. Phys.*, 2014, **141**, 044711.

77 N. R. Jaegers, J.-K. Lai, Y. He, E. Walter, D. A. Dixon, M. Vasiliu, Y. Chen, C. Wang, M. Y. Hu, K. T. Mueller, I. E. Wachs, Y. Wang and J. Z. Hu, Mechanism by which Tungsten Oxide Promotes the Activity of Supported V$_2$O$_5$/TiO$_2$ Catalysts for NO$_X$ Abatement: Structural Effects

Revealed by ^{51}V MAS NMR Spectroscopy, *Angew. Chem., Int. Ed.*, 2019, **58**, 12609–12616.

78 J. Yu, A. L. Godiksen, A. Mamahkel, F. Søndergaard-Pedersen, T. Rios-Carvajal, M. Marks, N. Lock, S. B. Rasmussen and B. Brummerstedt Iversen, Selective Catalytic Reduction of NO Using Phase-Pure Anatase, Rutile, and Brookite TiO_2 Nanocrystals, *Inorg. Chem.*, 2020, **59**, 15324–15334.

79 H.-S. Kim, S. A. Zygmunt, P. C. Stair, P. Zapol and L. A. Curtiss, Monomeric Vanadium Oxide on a θ-Al_2O_3 Support: A Combined Experimental/Theoretical Study, *J. Phys. Chem. C*, 2009, **113**, 8836–8843.

80 L. Arnarson, H. Falsig, S. B. Rasmussen, J. V. Lauritsen and P. G. Moses, The Reaction Mechanism for the SCR Process on Monomer V^{5+} Sites and the Effect of Modified Brønsted Acidity, *Phys. Chem. Chem. Phys.*, 2016, **18**, 17071–17080.

81 X.-F. Yang, A. Wang, B. Qiao, J. Li, J. Liu and T. Zhang, Single-Atom Catalysts: A New Frontier in Heterogeneous Catalysis, *Acc. Chem. Res.*, 2013, **46**, 1740–1748.

82 S. Liang, C. Hao and Y. Shi, The Power of Single-Atom Catalysis, *ChemCatChem*, 2015, **7**, 2559–2567.

83 G. C. Bond, Preparation and properties of vanadia/titania monolayer catalysts, *Appl. Catal., A*, 1997, **157**, 91–103.

84 G. Mul, M. A. Bañares, G. G. Cortéz, B. Van Der Linden, S. J. Khatib and J. A. Moulijn, MultiTRACK and operando Raman-GC study of oxidative dehydrogenation of propane over alumina-supported vanadium oxide catalysts, *Phys. Chem. Chem. Phys.*, 2003, **5**, 4378–4383.

85 E. Heracleous, M. Machli, A. A. Lemonidou and I. A. Vasalos, Oxidative dehydrogenation of ethane and propane over vanadia and molybdena supported catalysts, *J. Mol. Catal. A: Chem.*, 2005, **232**, 29–39.

86 A. Christodoulakis, E. Heracleous, A. A. Lemonidou and S. Boghosian, An operando Raman study of structure and reactivity of alumina-supported molybdenum oxide catalysts for the oxidative dehydrogenation of ethane, *J. Catal.*, 2006, **242**, 16–25.

87 B. Kilos, A. T. Bell and E. Iglesia, Mechanism and site requirements for ethanol oxidation on vanadium oxide domains, *J. Phys. Chem. C*, 2009, **113**, 2830–2836.

88 I. E. Wachs, Catalysis science of supported vanadium oxide catalysts, *Dalton Trans.*, 2013, **42**, 11762–11769.

89 L. J. Burcham, M. Badlani and I. E. Wachs, The origin of the ligand effect in metal oxide catalysts: Novel fixed-bed in situ infrared and kinetic studies during methanol oxidation, *J. Catal.*, 2001, **203**, 104–121.

90 G. Tsilomelekis, A. Christodoulakis and S. Boghosian, Support Effects on Structure and Activity of Molybdenum Oxide Catalysts for the Oxidative Dehydrogenation of Ethane, *Catal. Today*, 2007, **127**, 139–147.